

submitted to *Biophys. J.*
revised version
final version

March 28, 2008
April 22, 2008
May 20, 2008

This un-edited manuscript has been accepted for publication in Biophysical Journal and is freely available on BioFast at <http://www.biophysj.org>. The final copyedited version of the paper may be found at <http://www.biophysj.org>.

Soluble amyloid β oligomers affect dielectric membrane properties by bilayer insertion and domain formation: Implications for cell toxicity

Gintaras Valincius,¹ Frank Heinrich,^{2,3} Rima Budvytyte,¹ David J. Vanderah,⁴ Duncan J. McGillivray,⁵ Yuri Sokolov,⁶ James E. Hall,⁶ and Mathias Lösche^{2,3,*}

¹Department of Bioelectrochemistry and Biospectroscopy, Institute of Biochemistry, Vilnius, LT-08662, Lithuania

²Physics Department, Carnegie Mellon University, Pittsburgh, PA 15213-3890

³Center for Neutron Research, National Institute of Standards and Technology, Gaithersburg, MD 20899-6102

⁴Chemical Sciences and Technology Laboratory, National Institute of Standards and Technology, Gaithersburg, MD 20899-8313

⁵Department of Chemistry, The University of Auckland, Auckland 1142, New Zealand

⁶Department of Physiology and Biophysics, School of Medicine, University of California at Irvine, Irvine, CA 92697

Supporting Information available as a Supplementary File (PDF format) for *BJ Online*:

Figures 2–4 in color and evaluation of neutron reflection model parameter confidence limits by Monte Carlo resampling

*Correspondence:

Mathias Lösche,
Physics Department, Carnegie Mellon University, 5000 Forbes Ave., Pittsburgh, PA 15213-3890
412-268-2735, fax: 412-268-8252, emb: quench@cmu.edu

ABSTRACT

It is well established that Alzheimer's amyloid β peptides reduce the membrane barrier to ion transport. The prevailing model ascribes the resulting interference with ion homeostasis to the formation of peptide pores across the bilayer. In this work we examine the interaction of soluble prefibrillar amyloid β ($A\beta_{1-42}$) oligomers with bilayer models, observing also dramatic increases in ion current at μM peptide concentrations. We demonstrate that the $A\beta$ -induced ion conductances across free-standing membranes and across substrate-supported "tethered" bilayers are quantitatively similar and depend on membrane composition. However, characteristic signatures of the molecular transport mechanism were distinctly different from ion transfer through water-filled pores, as shown by a quantitative comparison of the membrane response to $A\beta$ oligomers and to the bacterial toxin, α -hemolysin (αHL). Neutron reflection from tethered membranes showed that $A\beta$ oligomers insert into the bilayer, affecting both membrane leaflets. By measuring the capacitance of peptide-free membranes as well as their geometrical thicknesses, the dielectric constants in the aliphatic cores of 1,2-dioleoyl-*sn*-glycero-3-phosphocholine (DOPC) and 1,2-diphytanoyl-*sn*-glycero-3-phosphocholine (DPhyPC) bilayers were determined to be $\epsilon = 2.8$ and 2.2 , respectively. The magnitude of the $A\beta$ -induced increase in ϵ indicates that $A\beta$ oligomers affect membranes by inducing lateral heterogeneity in the bilayers, but an increase of the bilayers' water content was not observed. The activation energy for $A\beta$ -induced ion transport across the membrane is at least 3x higher than that measured for membranes reconstituted with αHL pores, $E_a = 36.8$ vs. 9.9 kJ/mol, indicating that the molecular mechanisms underlying both transport processes are fundamentally different. The $A\beta$ -induced membrane conductance shows a nonlinear dependence on the peptide concentration in the membrane. Moreover, E_a depends on peptide concentration. These observations suggest that cooperativity and/or conformational changes of the $A\beta$ oligomer particles upon transfer from the aqueous to the hydrocarbon environment play a prominent role in the interaction of the peptide with the membrane. A model in which $A\beta$ oligomers insert into the hydrophobic core of the membrane—where they lead to a local increase in ϵ and a concomitant reduction of the membrane barrier—describes the experimental data quantitatively.

Key words:

Alzheimer's disease; membrane ion barrier; conduction mechanism; tethered bilayer lipid membrane; electrochemical impedance spectroscopy; neutron reflection

Running title: $A\beta$ oligomer effects on membrane ion barrier

Abbreviations:

A β : amyloid β

AD: Alzheimer's disease

APP: amyloid precursor protein

IAPP: islet amyloid polypeptide

PD: Parkinson's disease

HFIP: hexafluoroisopropanol

DMPC: 1,2-dimyristoyl-*sn*-glycero-3-phosphocholine

DMPC-d₅₄: 1,2-diperdeuteromyristoyl-*sn*-glycero-3-phosphocholine

DOPC: 1,2-dioleoyl-*sn*-glycero-3-phosphocholine

DPhyPC: 1,2-diphytanoyl-*sn*-glycero-3-phosphocholine

WC14: 20-tetradecyloxy-3,6,9,12,15,18,22-heptaohexatricontane-1-thiol

HEO: hexa(ethylene oxide)

HEPES: 4-(2-hydroxyethyl)-1-piperazineethanesulfonic acid

Tris: 2-amino-2-hydroxymethyl-1,3-propanediol

BLM: free-standing bilayer lipid membrane ("black" lipid membrane)

SAM: self-assembled monolayer

stBLM: sparsely-tethered bilayer lipid membrane

β ME: β -mercaptoethanol

α HL: α -hemolysin from *Staphylococcus aureus*

RBL: rat basophilic leukemia

EIS: electrochemical impedance spectroscopy

ECM: equivalent circuit model

CPE: constant phase element

NR: neutron reflectometry

nSLD: neutron scattering length density

AFM: atomic force microscopy

INTRODUCTION

The correlation between neurodegenerative disease and amyloid aggregation in brain tissue has long been established (1): Fibrillar plaques associated with dead or damaged neurons are a characteristic observation in postmortem brains of patients suffering from Alzheimer's and Parkinson's diseases (AD and PD, respectively). Consequently, the amyloid hypothesis links protein aggregation into fibrillar structures with a cascade of events that leads ultimately to neurodegeneration (2). However, the question whether the deposits are caused by, or rather lead to, neurodegeneration has been vigorously debated for a century and remains unanswered (3), at least partially due to the lack of a viable molecular-scale approach to its investigation.

One reason for the persistence of this debate lies in the variety of guises in which amyloid peptides and their aggregation products occur *in vivo*. Firstly, there is a variability in the cleavage sites in the proteolytic processing of the amyloid precursor protein (APP) by various secretases (4), yielding product peptides of different lengths, *i.e.*, $A\beta_{1-40}$ and $A\beta_{1-42}$. Secondly, their sequential oligomerization into larger aggregates leads to different physical forms – monomers, oligomers, protofibrils, fibrils and fibrillar tangles – that may be in dynamic equilibrium and may each contribute differently to pathogenicity. Much recent work was dedicated to structural characterization of amyloid aggregation products and attempts on unraveling their reactive pathways (5-9). Indeed, evidence has recently accrued that $A\beta$ toxicity resides primarily with a soluble oligomeric form of the peptide rather than $A\beta$ monomers or mature fibrils (10-17). In view of the lack in understanding of the molecular origin of $A\beta$ toxicity it is therefore timely to concentrate on molecular biophysical studies of the properties of $A\beta$ oligomer particles (18).

Because $A\beta$ peptides implicated in AD and the aggregation products of other misfolded peptides implicated in related peptide misfolding pathologies (19)—such as α -synuclein (PD), polyglutamine (Huntington's disease), islet amyloid polypeptide (IAPP, type 2 diabetes mellitus)—affect very different tissues in patients and because misfolded peptide oligomers appears to translocate membranes easily, it is intriguing to speculate that oligomer interaction with bilayer membranes play a major role in determining the physiological roles of these peptide oligomers on the molecular scale (4). In fact, soluble $A\beta_{1-42}$ oligomers destabilize the membrane of giant unilamellar vesicles (20). Not surprisingly, the poration of membranes by amyloid aggregates has been a major recurring theme in explaining amyloid toxicity ever since a first report of membrane channels induced by amyloid peptide was published (21). After all, membrane pores formed by amyloid oligomers or even specific channel structures similar to those formed by bacterial exotoxins, would greatly disturb Ca^{2+} homeostasis thereby providing a plausible mechanism for oligomer toxicity (22). The amyloid channel hypothesis has also been fueled by the observation of annular peptide aggregates, for example in AFM studies of substrate-supported membranes (23,24), that are suggestive of pore formation. However, the preparation protocol invokes self-assembly from premixed lipid/peptide solutions, raising doubts about their physiological significance, particularly because the incubation of preformed bilayers with amyloid solution yields peptide structures that are morphologically distinct (25).

Evidence for ion channels from membrane conductivity measurements is also not yet conclusive. On the one hand, there are reports of conductance patters in bilayers (23,26) and clamped cell membranes (27) that resemble the single channel behavior observed in exotoxin studies (28) in free-standing bilayers (black lipid membranes, BLMs – see Fig. 1A). On the other hand, in both BLMs and cultured rat basophilic leukemia (RBL) cells it was demonstrated that soluble $A\beta_{1-42}$ oligomers increase the conductance of membranes in a way inconsistent with the formation of ion channels (15,17). From these studies, the oligomers affect the lipid membranes by lowering the dielectric barrier of the bilayer. Most intriguingly, in the BLM studies which investigated compositionally well-defined lipid bilayers it was found that membranes composed

of lipids with high compressibility, such as phospholipids with unsaturated chains, are more amenable to peptide oligomer effects than those composed of low-compressible lipids, such as phospholipids with phytanoyl chains or sphingomyelins (17).

Beyond interference with ion homeostasis by conductance increases, subtle alterations of membrane properties may play more complex roles in AD etiology. Seelig and coworkers have early on recognized the interdependence of membrane exposure of A β and peptide conformation, see ref. (29) and work cited therein. McLaurin and coworkers have been investigating the role of membranes in peptide fibrillogenesis further (30). This line of research is continuing to date with progressively deeper insight into molecular details (31,32). Even more intriguing are aspects of membrane microstructure and their implications for disease. The role of lipid materials properties in the formation of microheterogeneity (“raft hypothesis”) has been recently reviewed (33) and their role in the recruitment of peptides discussed. In the context of AD, the role of “lipid rafts” in cell signaling may be of secondary relevance, but there have been reports implicating rafts in the amyloidogenic processing of APP by both β -secretase and γ -secretase (34-36). In the light of those findings, the interaction of A β with rafts becomes very relevant. Indeed, if A β peptide was to affect the formation or balance of microheterogeneities in affected membranes, this might provide a fatal amplification mechanism for pathogenesis.

Here we investigate supported membranes (37-39) for their structural and electrochemical response to soluble A β oligomers to study the molecular-scale events that govern A β oligomer interaction with bilayers. We have optimized a supported bilayer system, the sparsely tethered bilayer lipid membrane (stBLM, see schematic representation in Fig. 1B), in which a lipopolymer tether anchors a bilayer structure to the gold-coated surface of a Si wafer (40). Neutron reflectometry (NR) has been used to determine the molecular-scale structure of these systems. In the preparation of stBLMs, the tether molecules are laterally diluted by a hydrophilically terminated thiol, β -mercaptoethanol (β ME), resulting in a molecularly thin ($d \sim 15$ Å), stable hydration layer between the membrane and the gold layer (40,41). For biophysical work, stBLMs offer the advantage of a well-defined model system that is amenable to a multitude of well-established, molecular-scale characterization techniques. For example, stBLMs were structurally characterized in detail using NR (40). Equally important, the synergy between NR and electrochemical impedance spectroscopy (EIS) has been demonstrated (41). The combined metrologies couple structural characterization (NR) with the assessment of protein function in the membrane (EIS). For example, a recent investigation of the formation of nanoscale pores in stBLMs by the exotoxin, α -hemolysin (α HL) from *S. aureus* (42), with these techniques (43) enables a quantitative comparison of the impact of A β oligomers with that of α HL in this study. Taken together, these results on stBLMs also afford a comparison with the effects of A β oligomers on free-standing BLMs and cell membranes. In the context of Alzheimer’s etiology, this is important because monitoring membrane conductivity provides access to molecular details of the interaction between A β_{1-42} oligomers and the bilayer, whose dielectric properties are essential for the homeostasis of ions, as well as the passive and active ion transport that governs signal conduction along the axon. An increase of membrane permeability by A β oligomers conceivably affects a complex network of biochemical cascades, thus leading to a spectrum of pathological symptoms. A better understanding of molecular-level effects of A β oligomers on membranes is therefore critically needed for the development of early-detection mechanisms for AD, as well as for therapeutic approaches.

MATERIALS AND METHODS¹

Materials and sample preparation. 20-tetradecyloxy-3,6,9,12,15,18,22-heptaohexatricosane-1-thiol (WC14) was synthesized and characterized as described (supporting information for (40)). β ME, from Sigma-Aldrich (St. Louis, MO), was distilled before use. 1,2-diphytanoyl-*sn*-glycero-3-phosphatidylcholine, 1,2-dioleoyl-*sn*-glycero-3-phosphatidylcholine, 1,2-dimyristoyl-*sn*-glycero-3-phosphatidylcholine, and 1,2-perdeuterodimyristoyl-*sn*-glycero-3-phosphatidylcholine (DPhyPC, DOPC, DMPC and DMPC- d_{54} , respectively) were from Avanti Polar Lipids (Alabaster, AL). H₂O was purified in a Millipore (Billerica, MA) UHQ reagent-grade water purification system. D₂O (99.9% isotope purity) was from Cambridge Isotopes Laboratory (Andover, MA). Salts, buffers, organic solvents and squalene from Sigma-Aldrich, J. T. Baker or Mallinkrodt-Baker were at least of ACS reagent or analytical reagent grade.

Planar lipid bilayers. Free-standing BLMs were formed at room temperature by the union of two monolayers as previously described (15,17). Briefly, lipid monolayers were formed on aqueous solutions that contained various concentrations of KCl or NaCl buffered with 10 mM HEPES-Tris to pH 7.4. They were apposed over a hole (diameter \sim 150 μ m) in a 15 μ m thick Teflon partition dividing the two aqueous phases. The hole, punched by an electric spark, was precoated with a 2.5% solution of squalene in *n*-pentane. Bilayer formation was monitored by measuring capacitance. Silver/silver chloride electrodes were used to apply voltages and record currents across the bilayer. One chamber potential was taken as ground and additions were made to the other chamber. Solutions were stirred with magnetic stirring bars for about 30 s after additions. Voltages were generated and currents digitized at a resolution of 12 bits by an AD Lab ADC/DAC board controlled by JCLAMP (SciSoft Co., New Haven, CT) driving a PCI-6024E board (National Instruments, Austin, TX). Currents were transduced by an Axopatch 200A amplifier (Axon Instruments, Foster City, CA) connected to the board. For measurements of the membrane conductance, a voltage ramp protocol ($U = -150$ to $+150$ mV at 60 mV/s) was applied.

Tethered lipid bilayers. stBLMs were formed on thin gold films (thickness, \sim 10 nm for NR and \sim 200 nm for EIS), deposited by magnetron sputtering (Auto A306; BOC Edwards, UK) on *n*-doped, [100]-cut Si wafers (EI-Cat Inc., Waldwick, NJ, or Silicon, Inc., Boise, ID) precoated with a \sim 2 nm thick Cr adhesion layer, as described (44). Typically, the gold films had an RMS surface roughness of 0.5 nm, as measured by x-ray reflectometry (Bruker AXS, Madison, WI). Similar values were determined by AFM: \sim 0.5 nm for thin gold films and \sim 0.8 nm for the 200 nm gold films. The thickness uniformity across the surface was \pm 3% or better, as determined by ellipsometry.

The formation of stBLMs is a two-step process that involves the coadsorption of WC14 with β ME, followed by incubation with an ethanolic phospholipid solution and rapid solvent exchange (38): (1) Mixed self-assembled monolayers (SAMs) were prepared by exposing magnetron-sputtered Au films to solutions of WC14: β ME (3:7 mol:mol, 0.2 mM total concentration) in 99.5% ethanol for $>$ 12 h. (2) stBLMs were completed by incubation of the moderately hydrophobic surface with a concentrated (\sim 10 mM) ethanolic solution of a phospholipid which was rapidly, within \sim 5 s, replaced by vigorous injection of aqueous buffer (0.1 M NaCl, 0.01 M phosphate,

¹Certain commercial materials, instruments, and equipment are identified in this manuscript in order to specify the experimental procedure as completely as possible. In no case does such identification imply a recommendation or endorsement by the National Institute of Standards and Technology nor does it imply that the materials, instruments, or equipment identified is necessarily the best available for the purpose.

pH 7.0–7.5) into the sample cell. This rapid solvent exchange procedure leads to the formation of a complete and electrically insulating bilayer with a residual conductance of 1–2 $\mu\text{S}/\text{cm}^2$ (40).

Amyloid oligomer particles. $\text{A}\beta_{1-42}$ oligomers were prepared at UC Irvine as described (15,17). Lyophilized peptides were resuspended in 50% acetonitrile in water and re-lyophilized. Soluble oligomers were prepared by dissolving 1.0 mg of peptide in 400 μL hexafluoroisopropanol (HFIP) at room temperature. 100 μL of the resulting seedless solution was added to 700 μL H_2O in a siliconized Eppendorf tube. After 10–20 min. of incubation, samples were centrifuged for 15 min. at 14,000 $\times g$. The supernatant (pH 2.8–3.5) was transferred into a new siliconized tube and the HFIP evaporated in a gentle N_2 stream. Samples were then stirred at 500 rpm using a Teflon coated micro stir bar for 24–48 hr at room temperature. Aliquots were taken at 6–12 h intervals for testing in dot blots with the anti-oligomer antibody, A11 (14). Samples were also characterized using electron microscopy and size exclusion chromatography (45). Freshly prepared peptide oligomers were shipped overnight to NCNR for characterization in EIS and NR experiments. As described in detail below, the concentration dependence of $\text{A}\beta_{1-42}$ oligomers on EI spectra can be used to monitor oligomer activity. In split batches, the activity of oligomer preparations determined with EIS on stBLMs correlated well with the oligomer activity measured on free-standing BLMs at UC Irvine.

Electrochemical impedance spectroscopy. EIS measurements were performed using a Solartron (Farnborough, U.K.) system (model 1287A potentiostat and model 1260 frequency response analyzer) between 1.0 and 65,000 Hz with 10 logarithmically distributed measurements per decade. Data were fitted using ZView (Scribner Associates, Southern Pines, NC). Gold-coated silicon wafers (20 \times 40 mm) served as the working electrode in a setup that allowed simultaneous EIS measurements in 6 distinct electrochemical cells (volume, $V \sim 250 - 300 \mu\text{L}$) on each wafer, with their surface areas ($A_{el} \sim 0.33 \text{ cm}^2$) on the gold film confined by Viton O-rings. Copper contrast was used to measure the geometric electrode surface area (46). EIS data were normalized to A_{el} and the roughness factor β , estimated from the gold surface oxidation/oxide stripping charge (47). A saturated silver-silver chloride ($\text{Ag}|\text{AgCl}|\text{NaCl}(\text{aq}, \text{sat})$) micro-electrode (Microelectrodes, Bedford, NH, model M-401F) was used as reference. The auxiliary electrode was a 0.25 mm diameter platinum wire (99.99% purity, Aldrich) coiled around the barrel of the reference electrode. The distance between the tip of the reference and working gold electrode surface was set to 2 – 3 mm. All measurements were carried out at 0 V bias vs. the reference electrode at $21 \pm 1^\circ\text{C}$ in aerated solutions.

Neutron reflection, and data analysis. NR measurements were performed on the Advanced Neutron Diffractometer/Reflectometer (AND/R) (48) at the NIST Center for Neutron Research (NCNR). The resilience of the stBLMs permitted the NR characterization of the as-prepared membrane at various solvent contrasts, followed by measurement of the stBLM incubated with $\text{A}\beta$ oligomers, *all with the same physical sample*. Also, since the incubation with the peptide was performed *in-situ* on the neutron spectrometer, all reflectivity curves were measured on exactly the same sample footprint. With the substrate and membrane structures thus established in a first step, structural changes due to amyloid incubation were studied in detail.

All stBLMs were prepared with a single phosphatidylcholine species—DOPC, DPhyPC, DMPC, or DMPC- d_{54} . With hydrogenated phospholipid, the inner and outer bilayer leaflets are identical in nSLD, and cannot be discriminated. On the other hand, using DMPC- d_{54} enabled a discrimination of the stBLM leaflets because the outer leaflet is composed of 100% deuterated polymethylene whereas the inner leaflet is composed of a mixture of hydrogenated polymethylene (of the WC14) and of deuterated polymethylene (of DMPC- d_{54} intercalating the tethered WC14 SAM). Further neutron contrast is most easily achieved by using buffers of various isotopic compositions for the solution bathing the stBLM. We showed in earlier work that stBLMs are stable

(at least) over days and are also stable against buffer exchange. Exploiting this stability, each of the as-prepared stBLMs was sequentially characterized in three different solvent contrasts using buffer based upon D₂O, H₂O, or a mixture of both, e.g., with an nSLD, $\rho_n \sim 4 \times 10^{-6} \text{ \AA}^{-2}$ (“CM4”). This basic characterization of the neat stBLM was followed by continuous incubation with A β_{1-42} oligomers at the desired peptide concentration and further NR measurements with peptide solutions in buffers of different isotopic constitutions. Reversibility of the peptide interaction with the lipid bilayer was routinely probed in a final NR measurement that followed extensive rinsing.

Data analysis was performed in terms of slab models, or “box” models (49), using *ga_refl* (50), in which the reflectivity from a model neutron scattering length density (nSLD) profile is computed using an optical matrix formalism based on Parratt’s recursion algorithm (51). Isostructural samples with distinct isotopic contrast were simultaneously fitted by consistently refining the corresponding nSLD profiles which were parameterized in terms of the underlying molecular structures (52), an approach termed “composition-space refinement” (53). In the implementation used in this work, the model contains the following sequence of layers to represent the sample system: (semi-infinite) Si wafer, siliconoxide, chromium, gold, the hydrated hexa(ethylene oxide) (HEO) spacer, the inner leaflet of the bilayer, the outer leaflet of the bilayer, the outer headgroup layer, and bulk solvent. The model allows all organic layers to comprise solvent (thought to either hydrate organic moieties such as a phospholipid headgroups or to form solvent-filled defect pockets, as in the case of the hydrophobic chain layer). Thus solvent contributes to the average scattering power of each layer according to the nSLD of the bulk solvent multiplied by its volume fraction in the layer (which is zero for a defect-free stBLM). Both lipid leaflets in the stBLM model were constrained to the same hydrophobic thickness because in high-quality bilayers such as the ones investigated in this work, the two thicknesses are highly correlated. The inner headgroup layer of the lipid membrane was indistinguishable from the HEO tether at any solvent contrast, and was therefore not separately modeled.

The stability of the stBLMs was confirmed by the fact that any of the data sets at different solvent contrasts can be well described by the same parameter set in the refined composition-space model (40,41). Moreover, if data sets representing different neutron contrasts were fitted independently of each other, this yielded consistent parameter values, albeit with larger uncertainties. The final analysis of an experiment—reported in terms of best-fit parameters and associated uncertainties in the following section—was therefore always performed in a simultaneous fit to all reflectivity curves taken on a particular bilayer sample. In these results, *identical* parameter values describe those regions in the sample invariant to solvent exchange or peptide oligomer incubation (*i.e.*, the inorganic multilayer substrate). In distinction, regions that are solvent accessible and/or affected by the peptide are described by parameter sets which are *mutually consistent* in that they derive from a unique molecular structure that translates to distinct nSLDs by attaching the appropriate scattering lengths to its atomic composition.

RESULTS

Neutron reflection from tethered bilayer membranes. Only protonated $A\beta_{1-42}$ was available in these experiments. Because the peptides' contrast against the membrane structure is low, the particles could not be directly located at the membrane in a structural model. On the other hand, the membrane's structural properties were critically affected by $A\beta_{1-42}$ oligomer incubation which led to significant and reversible changes in the stBLMs' structural parameters. Here, we use this information for a quantitative assessment of the membranes' dielectric responses. Initial NR experiments with fully hydrogenated stBLMs suggested a small, reversible thinning of the hydrophobic core of the bilayers, which depended in its extent on the nature of the lipid, peptide concentration and the activity of the $A\beta_{1-42}$ oligomer preparation. Subsequent measurements employing chain-perdeuterated DMPC- d_{54} showed these changes in more detail. We will therefore in the following concentrate on experiments with the chain-labeled membrane component.

The stBLM prepared from DMPC- d_{54} was characterized with NR in an extended set of measurements. The as-prepared membrane was first characterized at 3 solvent contrasts, then subjected to soluble $A\beta_{1-42}$ oligomers at $c_p = 2 \mu\text{M}$ in D_2O -based buffer and characterized at 2 more solvent contrasts; subjected to $c_p = 6 \mu\text{M}$ and characterized at 3 more solvent contrasts; subjected to $c_p = 12 \mu\text{M}$ and characterized at 2 more solvent contrasts; it was finally rinsed with peptide-free buffer, and characterized again at 3 solvent contrasts. The entire experiment used ~ 4 days of neutron beamtime. In Fig. 2, we present exemplary NR data sets measured in H_2O -based buffer, as well as the respective model fits, for the neat stBLM and the same stBLM incubated with soluble $A\beta_{1-42}$ oligomers at the final peptide concentration of $c_p = 12 \mu\text{M}$. The normalized residuals, shown in an inset at the bottom of the graph, emphasize the reflectivity changes inferred by the peptide oligomers. They also demonstrate the almost complete reversal of those effects upon rinsing with peptide-free buffer. Because the stBLM was prepared from (fully hydrogenated) WC14: β ME (3:7 in the adsorption solution) and completed with DMPC- d_{54} , the inner and the outer hydrophobic sheath of the bilayer show different nSLD. In Fig. 2, they are well distinguished in the nSLD profiles shown in the top inset. A close inspection of these profiles shows that $A\beta$ oligomer incubation increases the nSLD of the hydrophobic slabs, and shifts the peak nSLD closer to the substrate surface. Table 1 lists the model parameters obtained from a simultaneous fit to all NR data. A more complete account that includes the inorganic substrate and confidence limit estimates based on a Monte Carlo resampling technique is provided online as *Supplemental Material*.

The bilayer shows no increase of solvent content in the hydrophobic slabs that would indicate the formation of solvent-filled defects in the bilayer by the peptide. The initial nSLD of the inner and outer leaflets were $\rho_n = 1.60 \pm 0.13 \times 10^{-6} \text{ \AA}^{-2}$ and $\rho_n = 5.55 \pm 0.34 \times 10^{-6} \text{ \AA}^{-2}$, respectively. The difference derives from the fact that the inner leaflet incorporates the (hydrogenated) lipid anchor, WC14. Assuming an alkyl nSLD of $\rho_n = -0.4 \times 10^{-6} \text{ \AA}^{-2}$, typical for chains in a fluid bilayer, and equal mass densities in the inner and the outer leaflet, we estimate the volume fraction of DMPC- d_{54} in the *inner* lipid leaflet to be $34 \pm 4\%$ in the as-prepared stBLM. Incubation with soluble $A\beta_{1-42}$ oligomers led to significant changes of the nSLD in both lipid leaflets for all peptide concentrations applied in the experiment. As for fully hydrogenated DOPC-based stBLMs (see below), we observe a thinning of the membrane. For the deuterated bilayer, this thinning amounts to $\Delta d = -1.4 \pm 0.4 \text{ \AA}$ and $-3.0 \pm 0.4 \text{ \AA}$ at $c_p = 6 \mu\text{M}$ and $c_p = 12 \mu\text{M}$, respectively. The material density of the headgroup (*i.e.*, its volume fraction within the layer next to the bulk solvent) increased by $8 \pm 4\%$, independent of the peptide concentration. Upon rinsing with buffer, all structural effects inferred by $A\beta_{1-42}$ oligomers on the stBLM were reversible within the confidence limits of the experiment. Trial models that included an adsorbed peptide layer at the interface between the bilayer headgroups and the bulk solvent did not indicate any significant

volume fraction of adsorbed material for any of the peptide concentrations.² This suggests that the peptide is not peripherally adsorbed to the membrane surface or inserted into the membrane while extending into the adjacent buffer. Rather, the model suggests that peptide oligomers insert more or less fully into the hydrophobic membrane core.

In terms of nSLD changes, fully hydrogenated stBLMs based upon DOPC and DPhyPC showed smaller responses than deuterated stBLMs to the incubation with $A\beta_{1-42}$ oligomers. Complex data sets that were collected in procedures similar to that described above for DMPC-d₅₄-based stBLMs, and are partially presented in Figs. 3 and 4. The corresponding model fits are given in Tables 2 and 3. These models show that nSLDs show little response to peptide incubation. The one notable exception concerns the nSLDs of the hydrophobic bilayer interior, which increased slightly due to peptide insertion. On the other hand, comparison of the nSLD profiles in different solvent contrasts shows unmistakably that peptide incubation didn't affect the water content of the bilayers: Consistent with the DMPC-d₅₄ results, both leaflets in both the DOPC and DPhyPC bilayers remained solvent-free within an uncertainty of 3%.

A significant difference in structural response of DPhyPC and DOPC to peptide incubation was observed in terms of the membrane thickness, which remained constant for DPhyPC whereas it decreased substantially for DOPC. Peptide concentrations of $c_p = 6 \mu\text{M}$ and $12 \mu\text{M}$ reduced the DOPC membrane thickness by $\Delta d = -2.4 \text{ \AA}$ and -3.8 \AA , respectively. This is substantially more than the thickness reduction observed for the saturated phospholipid, DMPC. As with DMPC stBLMs, the thinning relaxed completely after rinsing of the bilayer with aqueous buffer.

Electrochemical impedance spectroscopy of tethered bilayer lipid membranes. Incubation of stBLMs with soluble $A\beta_{1-42}$ oligomers results in spectral changes exemplified in Bode diagrams presented in Fig. 5 for DOPC. $A\beta$ leads to a characteristic reduction of the membrane impedance, Z , at low frequency, f (Fig. 5A). The onset of the associated plateau in $|Z(f)|$ coincides with a maximum of the phase angle, φ (Fig. 5B) and occurs at progressively higher f as c_p increases. Similar spectral signatures have been reported following membrane incubation with ionophores (38,54), pore-forming toxins (55) and phospholipase (41), which all increase the conductivity of membranes.

EI spectra were modeled using the equivalent circuit model (ECM) shown in the inset in Fig. 5. The stBLM is represented by a constant phase element (CPE_{stBLM}), whose impedance is defined as

$$Z_{CPE} = 1 / \left(i \left(|CPE| (i\omega)^\alpha \right) \right) \quad (1),$$

where $|CPE|$ and α are the coefficient and the phase of the constant phase element, i is the imaginary unit, and $\omega = 2\pi f$ is the cyclic frequency. The relevance and significance of this model was discussed earlier (40). Confidence limits of the parameters are quantified by the covariance matrices of the Levenberg-Marquardt algorithm employed in the nonlinear χ^2 minimization. Representative results of the modeling for DOPC-based stBLMs are shown in Table 4. The mean values of $|CPE|$ and α for the as-prepared stBLMs are $0.676 \pm 0.015 \mu\text{Fcm}^{-2}\text{s}^{\alpha-1}$ and 0.987 ± 0.002 , respectively, determined from $n = 29$ independent measurements. The value of α suggests that the stBLMs exhibit nearly ideal capacitive behavior, and therefore, $CPE_{stBLM} \approx C_{stBLM}$, the membrane capacitance. A detailed interpretation of these results in connection with

²The detection limits are estimated to be $< 10\%$ for the volume fraction and $\sim 10 \text{ \AA}$ for the thickness of such a hypothetical peptide layer.

structural data obtained from NR experiments enables us then to deduce molecular-scale models for the impact of A β oligomers on membrane properties, as presented in the Discussion section.

It has been reported that amyloids induce conductance pathways through membranes (21,23,24). These defects were interpreted as being similar to those created by ionophores such as gramicidin (38) or ion channels such as α HL (28). In the ECM in Fig. 5, such pathways are represented by another constant phase element (CPE_{def}) in series with a resistor, R_{def} . As shown earlier, such a model describes well the intrinsic conductance properties of functionally reconstituted α HL ion channels in stBLMs (43). Hence, the conductance,

$$Y_{A\beta} = R_{def}^{-1} \quad (2)$$

may be a reasonable descriptor of changes in the transport properties of the membrane inferred by soluble A β_{1-42} oligomers. The conductance, $Y_{A\beta}$, and membrane capacitance, C_{stBLM} , of stBLMs completed with DOPC are plotted in Fig. 6 as a function of c_p , the peptide concentration *in the aqueous bulk reservoir*. C_{stBLM} is linear in c_p . Because membrane thinning is negligible in this concentration range (see Table 1), any rise in C_{stBLM} derives from an increase of the membrane's dielectric constant, ϵ_{hc} , due to insertion of peptide, which has a higher permeability than alkane. This suggests that C_{stBLM} is also linear to c_p^{stBLM} —the peptide concentration *within the membrane*—and consequently $c_p^{stBLM} \propto c_p$. On the other hand, Fig. 6 shows that $Y_{A\beta}$ is nonlinear in c_p , and therefore presumably also nonlinear in c_p^{stBLM} . In fact, the isotherm deviates significantly from Langmuir-type behavior, both in stBLMs and free-standing BLMs: $Y_{A\beta}^{-1}$ vs. c_p^{-m} is linear for $m \approx 2$ (instead of $m = 1$, as expected for a Langmuir isotherm), suggesting cooperative effects and/or conformational changes of the A β_{1-42} oligomer particles as they transfer from the aqueous to the hydrocarbon environment.

Conductance of free-standing bilayer lipid membranes. Figure 7 shows A β oligomer-induced current-voltage (I - U) curves through free-standing BLMs as a function of temperature. All curves show the typical exponential shape for activated charge translocation with nearly linear portions near the origin ($|U| \leq 30$ mV, see inset). This inner part of the curves was used to estimate the zero-voltage conductances of the BLMs. Representative data are summarized in Table 5. The increase of the A β -induced conductance is superlinear, and a strong temperature dependence—a factor of ~ 2 per 10°C —indicates a high activation energy of the ion transfer through the membrane.

The ion current induced by A β oligomers across free-standing BLMs was measured as a function of lipid composition. Figure 8 displays bilayer currents, $I_{A\beta}$, vs. c_p , for DOPC, DPhyPC and their equimolar mixture. Their c_p dependence is superlinear, with $I_{A\beta}^{-1}$ vs. c_p^{-m} linear for $m \approx 2.3$, quantitatively similar to those observed with stBLMs (Fig. 6). Just as the stBLM response as a function of membrane composition seen in NR, the peptide-induced induced currents also show a strong dependence on the phospholipid chain constitution. As the membrane composition is changed from DPhyPC to DOPC, the induced currents increase by a factor of ≈ 20 for a given c_p . Similar effects were observed in the EI spectra of stBLMs for which the differences between saturated and unsaturated chains were smaller, however, amounting only to a factor of 3–4 (data not shown).

Activation energies of ion transfer across membranes. In view of the remarkable temperature dependence of the ion transport through BLMs shown in Fig. 7, EI spectra of stBLMs affected by soluble A β_{1-42} oligomers were also determined as a function of T . As with BLMs, a temperature increase leads to pronounced increases of stBLM conductances (see Fig. 9).

Specifically, both the plateau in the $|Z(f)|$ plot and the phase minimum move toward higher frequencies (data not shown). Modeling of the spectra enables a determination of R_{def} and consequently an assessment of the temperature-dependence of the conductance changes in the stBLMs.

Temperature effects on stBLM and BLM conductances were determined at $c_p = 1.6 \mu\text{M}$ for stBLMs and $c_p = 1$ and $2 \mu\text{M}$ for BLMs. Results are summarized in Fig. 9 and quantified in Table 6. In the figure, Arrhenius plots of stBLM and BLM conductances in the presence of $A\beta_{1-42}$ oligomers are compared with those for the ion transport in bulk electrolyte and across stBLMs reconstituted with αHL .³ These slopes yield activation energies for the ion conductance in the presence of $A\beta_{1-42}$ oligomers of $E_a \approx 37 \text{ kJ/mol}$ for a DOPC stBLM; for free-standing DOPC BLMs, $E_a \approx 46 \text{ kJ/mol}$ at $1 \mu\text{M}$ peptide and $E_a \approx 33 \text{ kJ/mol}$ at $2 \mu\text{M}$ peptide (see Table 6). These values are much lower than the activation energies for bare ions to cross neat lipid bilayers, but much larger than those for ion transport in bulk water. In comparison, the activation energy for ion transport through αHL is also significantly lower, $E_a \approx 10 \text{ kJ/mol}$ —closer to the value for ion transport through bulk solvent. E_a for the $A\beta$ -induced membrane conductivity itself depends pronouncedly on peptide concentration. In connection with the nonlinear relation, $Y_{A\beta}(c_p)$, shown in Fig. 6, this suggests that the amyloid properties within the membrane change in a concentration dependent manner.

DISCUSSION

The different model systems investigated in this work and the measurement techniques employed in their study are well connected. The combined application of EIS and NR is highly synergetic and provides insight into physical models of the bilayers, and the direct comparison of conductivity measurements and EIS link ion transfer across free-standing bilayers and surface-stabilized membranes. As we show below, there is quantitative agreement between these results. The biophysical effects we report here occur at similar $A\beta$ concentrations at which characteristic increases in the membrane conductance of patch-clamped cells were reported (15,17). Moreover, shifts of the gating properties of voltage-dependent channels (56), as well as cells lysis in tissue culture (57) occur at similar peptide concentrations. We therefore argue that the mechanism by which $A\beta$ oligomers induce electrical and structural changes in membranes may bear significance for the understanding of the toxic effects exerted on cellular systems. We will first discuss structural implications of the NR results, then proceed to discuss more quantitatively the electrical effects of $A\beta$ oligomers on membranes and finally comment on implications of these results for our understanding of the mechanism by which $A\beta$ affects membranes, specifically in the light of the amyloid channel hypothesis.

³BLM data for $c_p = 1 \mu\text{M}$ are omitted from Fig. 9 for clarity. BLM and stBLM experiments with $A\beta_{1-42}$ oligomers were conducted on bilayers formed with DOPC, because their response to the peptide is significantly larger than that of membranes based on DPhyPC (see Fig. 8). In contrast, αHL was studied in DPhyPC-based stBLMs, because αHL reconstitution has been most thoroughly studied into such membranes in a different investigation 43. McGillivray, D. J., G. Valincius, F. Heinrich, J. W. F. Robertson, D. J. Vanderah, W. Febo-Ayala, I. Ignatjev, M. Lösche, and J. J. Kasianowicz. 2007. Functional reconstitution of *Staphylococcus aureus* α -hemolysin in tethered bilayer lipid membranes. *Proc. Natl. Acad. Sci. USA*:submitted.. From these studies, we concluded that the reconstituted protein forms fully active membrane pores in the stBLMs which introduce narrow, water-filled channels into bilayers 42. Song, L., M. R. Hobaugh, C. Shustak, S. Cheley, H. Bayley, and J. E. Gouaux. 1996. Structure of staphylococcal α -hemolysin, a heptameric transmembrane pore. *Science* 274:1859-1865.. Attempts to reconstitute αHL into DOPC-based stBLMs have so far not been successful in our lab.

Both bilayer leaflets respond similarly to peptide incubation. Figure 10 shows changes in nSLD (Fig. 10A) and bilayer thickness (Fig. 10B) of deuterated stBLMs due to their exposure to soluble A β oligomers. Because the thickness parameters for the inner and outer leaflets were observed to be highly correlated in the fits, they were constrained to be identical in the model. On the other hand, the nSLDs of the two leaflets, well discriminated due to their distinct isotopic composition, develop differently as a function of c_p . However, this apparent difference vanishes if one compares the scattering length area density,

$$\rho_n^a = \rho_n \times d \quad (3),$$

which is a measure of inserted material per unit area and is shown in Fig. 10C as a function of c_p . The nearly perfect coincidence of ρ_n^a in both leaflets at any peptide concentration indicates that both monolayers are similarly affected by the peptide.

From these results, the impact of A β_{1-42} oligomers on the DMPC-d₅₄ bilayer can be summarized as follows: At $c_p = 2 \mu\text{M}$, no geometrical changes of the membrane are detected. However, the nSLD of both lipid leaflets rises by $0.29 \pm 0.09 \times 10^{-6} \text{ \AA}^{-2}$. This shows conclusively that there is incorporation of peptide material into the membrane, accompanied by an increase of the lipid packing density. Because the peptide nSLD is substantially lower than that of perdeuterated alkane, a mere replacement of lipid by peptide would be expected to reduce the nSLD of the bilayer core. Figure 10A shows that the opposite is true. Assuming the peptide nSLD to be $\rho_n = 2.1 \times 10^{-6} \text{ \AA}^{-2}$, the volume fraction of peptide material within the bilayer is estimated to amount to $\sim 14\%$.⁴ The nSLD of the outer lipid leaflet increases further by $\Delta\rho_n = 0.49 \pm 0.11 \times 10^{-6} \text{ \AA}^{-2}$ upon raising the peptide concentration in the buffer to $6 \mu\text{M}$, and saturates at this level. On the other hand, the nSLD of inner lipid leaflet decreases gradually from its peak value reached at $c_p = 2 \mu\text{M}$. This difference in behavior of the two membrane leaflets is a consequence of the thinning of the membrane and the distinct starting values of the nSLDs in both leaflets due to different degrees of deuteration. The apparent discrepancy is reconciled if one evaluates the neutron scattering length area densities: ρ_n^a is expected to change equally in both leaflets if they are affected by the same influx or outflux of deuterated lipid (which is the only mobile lipid species). This is indeed observed, as shown in Fig. 10C. In conclusion, this experiment shows unmistakably that (1) peptide material inserts into the membrane in significant amounts; (2) it affects both bilayer leaflets similarly; (3) lipid is not just replaced by the peptide but rather compacted in its local density – at least on average within the plane of the membrane.

NR results for the incubation of fully hydrogenated stBLMs with soluble A β_{1-42} oligomers (Figs. 3 and 4) showed small nSLD increases in response to peptide exposure (Tables 2 and 3). These changes are consistent with the interpretation, derived from results with deuterated stBLMs, that A β oligomer incorporation into the membrane increases the lipid density. However, such a conclusion cannot be drawn from the DOPC and DPhyPC data alone, because both a peptide induced lipid compaction the displacement of hydrogenated lipids by peptide without compaction are expected to result in an nSLD increase of a fully hydrogenated lipid bilayer.

⁴This model assumes that the number of lipids per unit area remains constant. However, a fluid bilayer may respond to peptide-induced changes in lipid conformation—affecting the area per lipid—with lateral flow, depositing excess lipid in reservoirs at defect sites (or retrieving material from such sites). For example, if due to a peptide-induced increase in local disorder lipid material expanded laterally, the estimate for ρ_n^a is too low.

Conversely, the estimate is too high if peptide insertion leads to lipid compaction. Exposure to increasingly larger amyloid concentrations will in that case eventually lead to a situation where membrane compaction can no longer be compensated for by the influx of lipid along the bilayer plane—which might explain the observed membrane thinning at $c_p = 6 \mu\text{M}$ and $c_p = 12 \mu\text{M}$.

Reversibility of $A\beta_{1-42}$ oligomer effects on membranes upon rinsing. As the residual plots in Figs. 2–4 and Fig. 10 show, the structural impact of $A\beta_{1-42}$ oligomers on membranes is almost perfectly reversible upon rinsing. Similarly, conductivity increases of bilayer induced by the peptide are largely reversed by simply rinsing the membranes with buffer, consistent with earlier reports (17). Moreover, it has been shown that most adverse effects of $A\beta_{1-42}$ oligomers on membrane and cell models – and even *in vivo* effects – can be avoided, or even reverted, by exposure to the oligomer-specific antibody, A11, developed in the Glabe lab (14). While we do not yet have a detailed molecular-scale picture of the interaction of $A\beta$ oligomers with the membrane due to the lack of NR experiments with deuterated peptide, these findings suggest an intriguing and unusual propensity for adaptation of the peptide aggregates to either of the aqueous and hydrophobic milieus. Clearly, upon transferring from buffer to the membrane interior, $A\beta$ oligomers must undergo conformational and/or aggregation changes to adapt to the different natures of these molecular environments. The apparent ease of peptide clearance from the membrane, presumably connected with a redispersion into aqueous buffer, then indicates that this interconversion cannot be associated with a large energetic barrier. Unfortunately, the lack of more detailed structural information prevents us from drawing more rigorous conclusions at this time.

Dielectric membrane properties and mechanisms that may compromise barrier function. Earlier results (17) as well as those presented here suggest that the increased ion conductance of membranes affected by $A\beta$ oligomers results from a breakdown of the dielectric barrier that prevents charged species from crossing the lipid bilayer. What is the mechanism of this dielectric breakdown? At least four scenarios are conceivable: (i) Pore or channel formation by $A\beta$ oligomers in the membrane. (ii) A mere thinning of the membrane (without the formation of pores), as observed with NR at $c_p > 2 \mu\text{M}$ (see Fig. 10), could increase ionic permeability. (iii) Because proteinaceous material has a larger ϵ than alkane, incorporation of $A\beta$ oligomers into the membrane may elevate ϵ_{hc} , thus reducing the energetic barrier for ion transport. (iv) $A\beta$ incorporation into the membrane could also introduce water and increase ϵ . Even if this would not lead to the formation of contiguous, membrane-spanning water-filled channels, such water-filled pockets might be even more effective than scenario (ii) in reducing the energy barrier.

The formation of membrane pores has been a recurring theme in the explanation of the observed increases in bilayer conductivity following incubation with $A\beta$ (21-24,58-60). This possibility has therefore been thoroughly considered in the data interpretation. However, for the membrane model systems and experimental conditions employed here, this scenario is not consistent with the experimental results, even if at first sight circumstantial evidence appeared to point toward channel formation.

For example, our observation of membrane thinning accompanying a conduction increase might be interpreted to be a result of amyloid channel formation, as reports in the literature show that pore-forming antimicrobial peptides lead to similar effects (61-63). Nevertheless, the nature of the conductance increase in the systems investigated here is dramatically different from those in other systems that have been interpreted as being due to channel formation (15,17). Moreover, NR do not indicate any increase of water content in the bilayers. While narrow pores at low concentration in a bilayer may not increase their water content sufficiently to be detected by NR, the activation energy of ion transport across the bilayer (Fig. 9 and Table 6) all but rigorously exclude channel formation in the BLMs and stBLMs we have studied. As suggested from its crystal structure (42) and verified in electrophysiology experiments (28), αHL forms well-defined water-filled pores in phospholipid bilayers. Ion transport through αHL pores are characterized by about the same activation energy ($E_a \approx 10 \text{ kJ/mol}$) as ions moving freely in solution bulk ($E_a \approx 5 \text{ kJ/mol}$). In distinction, the ion conduction through $A\beta$ -induced pathways has a significantly

higher activation energy ($E_a \approx 46\text{--}33$ kJ/mol for stBLMs and BLMs, both composed of DOPC, in the concentration range of 1–2 μM peptide), suggesting a fundamentally different mechanism. As shown in Table 6, the activation energy observed for $A\beta_{1-42}$ oligomers is not only 3x higher than that measured with αHL , but is also significantly higher (more than 2x) than that reported for a different pore, gramicidin D (64), which forms narrower pores with 3–4 Å diameter (65,66) than αHL (~10 Å). Therefore, we dismiss the formation of pores as the origin of the increase in ion conductivity across the membrane in the model systems studied here under the experimental conditions used.

Similarly, by virtue of the NR results we can dismiss scenario (iv), the possibility that water inclusions contribute significantly to an increase in the dielectric constant of the bilayer. Changes of the water content in the bilayers were < 1%, if any, as judged from the models displayed in Tables 1–3. One percent of water in the bilayer would increase the dielectric constant, ϵ , by < 0.8—too little to account for the observed increase in membrane current, as we show below.

Before discussing in detail the most likely amyloid-induced ion transport mechanism(s), we quantify in more detail the dielectric properties of the membrane. Using the membrane thickness derived from NR, we estimate the dielectric constant, ϵ_{hc} , of the hydrophobic membrane slab as follows. The capacitance of the stBLM is composed of serial contributions from the hydrocarbon (*hc*) slab and the Helmholtz (*H*) capacitance:

$$C_{stBLM}^{-1} = C_{hc}^{-1} + C_H^{-1} \quad (4)$$

On the basis of an approximate value for C_H of $6.25 \pm 0.12 \mu\text{Fcm}^{-2}$ with $\alpha = 0.992 \pm 0.001$ ($n = 10$), determined earlier, and the experimental result for C_{stBLM} , we calculate $C_{hc} \approx 0.76 \mu\text{Fcm}^{-2}$. Using Eq. 5,

$$\epsilon_{hc} = \frac{C_{hc} \times d_{hc}}{\epsilon_0} \quad (5)$$

C_{hc} in connection with the experimentally measured thickness, $d_{hc} = 32.8 \pm 0.5$ Å, yields $\epsilon_{hc} \approx 2.8$ for DOPC. An analogous estimate for DPhyPC yields $\epsilon_{hc} \approx 2.2$, consistent with the distinct nature of the unsaturated and saturated chains. In what follows, these results for ϵ_{hc} will serve as an experimentally determined basis for the quantification of $A\beta$ oligomer-induced changes of dielectric membrane properties.

Figure 6 shows that a pronouncedly nonlinear increase in $Y_{A\beta}$ is accompanied by an increase in C_{stBLM} that is linear in c_p . Because α remains close to unity (Table 4), $CPE_{stBLM} \approx C_{stBLM}$ at all c_p . At $c_p = 1.6 \mu\text{M}$, $C_{stBLM}^{A\beta} = 0.74 \pm 0.02 \mu\text{F/cm}^2$, and with Eqns. (4) and (5), $C_{hc}^{A\beta} = 0.84 \pm 0.02 \mu\text{F/cm}^2$ for DOPC membranes affected by $A\beta$ oligomers, an increase in membrane capacitance by $\approx 13\%$.

Because we dismissed the channel scenario, this $A\beta$ -induced conductance increase may be due to either membrane thinning or an increase in ϵ_{hc} , or both. Membrane permeability and conductance both scale with the geometric barrier thickness as d_{hc}^{-1} (67,68). In addition, membrane thinning may also affect permeability by lowering the barrier for ion penetration into the hydrophobic core of the bilayer. Image charge effects are the main reason for this reduction but don't change the barrier height significantly in the membrane thickness regime, $d_{hc} \approx 30$ Å

(68,69).⁵ For example, from the data in Fig. 2 of (68) we estimate that the hydrophobic barrier is lowered by only 5% as d_{hc} decreases from 60 to 40 Å. In comparison, geometric changes of the bilayer are much smaller here. As seen in Fig. 10, a measurable reduction of d_{hc} is only observed at $c_p > 2 \mu\text{M}$ for DMPC. The situation is similar for stBLMs composed of DOPC, where geometrical changes of the membrane were smaller than the confidence limits at $c_p \leq 2 \mu\text{M}$. Consequently, one may with confidence exclude geometric changes of the bilayer thickness as the source of the observed increase in CPE. Therefore, we continue by analyzing quantitatively the possibility of changes of ϵ_{hc} by peptide insertion as the origin of dielectric breakdown of the membrane barrier.

A uniform increase in membrane dielectric constant is inconsistent with the observed conductivity increase. The dielectric constant, ϵ_{hc} , has a profound effect on ion permeability across the membrane because of the exponential dependence of the transfer rate on barrier height (71). For monovalent ions, Eq. (6) shows that the ΔG depends on ϵ_{hc} as

$$\Delta G_{\text{barrier}} = \frac{e^2}{8\pi\epsilon_0 r_{\text{ion}}} \left(\frac{1}{\epsilon_{hc}} - \frac{1}{\epsilon_w} \right) - \frac{e^2}{4\pi\epsilon_0 \epsilon_{hc} d_{hc}} \ln \left(\frac{2\epsilon_w}{\epsilon_w + \epsilon_{hc}} \right) \quad (6)$$

where ϵ_w is the dielectric constant of bulk water, e is the elementary charge and r_{ion} is the ion radius. Equation (6) accounts only for electrostatic contributions to the energy required for transferring an ion into a hydrophobic medium—the Born self-energy—(first term) and a finite-size correction for the hydrocarbon thickness (second term) (68,69). For an order-of-magnitude estimate of A β -induced ionic conductance changes, it is sufficient to account only for electrostatic contributions.

From the barrier height one may then further estimate the membrane conductance for monovalent ions:

$$Y = \frac{c_{\text{ion}} F^2}{RT} \frac{\gamma_+ D_+ + \gamma_- D_-}{d_{hc}} \quad (7)$$

where c_{ion} is the concentration of the electrolyte, R and F are the gas and Faraday constants, respectively, T is temperature, and γ and D are the partition coefficients and diffusion constants of ions in the membrane. For an ion k , γ is defined as:

$$\gamma_k = \exp(-\Delta G_k / RT) \quad (8).$$

As quantified above, A β_{1-42} oligomers increase the capacitance of the hydrocarbon membrane core by 13% at $c_p = 1.6 \mu\text{M}$. For the DOPC-based stBLM, Eq. (4) then predicts an increase in ϵ_{hc} from 2.8 to 3.2. On the other hand, for $\epsilon_{hc} = 3.2$, Eq. (6) yields an energy barrier, e.g. for chloride anions, $E_a = 107 \text{ kJ/mol}$,⁶ which would leave the membrane practically impermeable. The ionic

⁵Below $d_{hc} = 10 \text{ \AA}$, the membrane would not provide an appreciable barrier to ion flux (70. De Levie, R. 1978. Mathematical modeling of transport of lipid-soluble ions and ion-carrier complexes through lipid bilayer membranes. *Adv. Chem. Phys.* 37:99-137.). However, our statement refers to membranes with thicknesses in the range, $d_{hc} = 25 - 30 \text{ \AA}$.

⁶Using $r_{Cl^-} = 0.181 \text{ nm}$, $d_{hc} = 3.28 \text{ nm}$ (Table 2), $T = 293 \text{ K}$, $c = 10^{-4} \text{ mol/cm}^3$, and $\epsilon_w = 80$, the barrier for Na^+ ions is higher by a factor of ~ 1.8 . Therefore, we assume that Na^+ does not significantly contribute to membrane conductance. We note that this assumption may not be generally valid, because it is not clear whether or not Na^+ dehydrates fully upon partitioning into amyloid-affected membrane domains. Indirectly,

conductance of such a membrane in 0.1 M NaCl solution would be $Y \ll 1 \mu\text{S}/\text{cm}^2$, well below the experimentally observed result. A compelling conclusion from this inconsistency is that A β oligomers cannot affect the membrane's dielectric properties uniformly but must exert their impact *locally*, e.g. by the formation of domains where lipids in contact with the peptide may have different properties from lipids far away. Evidently, the increase of ϵ within A β -induced membrane domains is bound to be much larger than the expected increase in a hypothetical uniform adsorption model, i.e., $\epsilon_{hc}^{domain} \gg 3.2$.

The actual value of the average membrane dielectric constant under the influence of peptide, $\epsilon_{hc}^{A\beta}$, may be estimated by assuming that both A β -induced domains and unaffected areas contribute to the membrane capacitance in parallel. If so,

$$\epsilon_{hc}^{domain} = \epsilon_{hc}^{A\beta} \frac{(\xi - 1) + \theta}{\theta} x \quad (9)$$

may be used to estimate the resulting change in ϵ within a peptide-induced domain. In Eq. (9), θ is the area fraction of membrane domains, $\xi = C_{A\beta}/C_{hc}$ is the ratio of specific capacitances within and outside of the membrane domains and $x = d_{A\beta}/d_{hc}$ is the corresponding thickness ratio.

Implications for membrane physiology. As discussed above, the EIS data yield an estimate of $\xi = 1.13$ at $c_p = 1.6 \mu\text{M}$. Independently, NR results show that x in Eq. 9 is ~ 1 at low c_p for stBLMs of all compositions investigated here. The largest uncertainty concerns the estimate of θ , which cannot be derived with comparable precision from the available data. The most precise NR results—those that involve chain-perdeuterated DMPC—suggest $\sim 14\%$ of peptide material by volume inside the membrane at $c_p = 2 \mu\text{M}$, if one assumes that the lipid area density in the membrane remains constant; for (hydrogenated) DOPC and DPhyPC, NR results are even less precise. On the other hand, an estimate of θ may be obtained by using the experimentally measured activation energy, $E_a = 36.8 \text{ kJ/mol}$, as an approximate measure of $\Delta G_{barrier}$,⁷ and determining $\epsilon_{hc}^{domain} = 8.6$ from Eq. (6). With this value for ϵ_{hc}^{domain} , Eq. (9) yields $\theta \approx 0.06$.

A decrease in barrier height from $\Delta G_{barrier} \gg 100 \text{ kJ/mol}$ for a neat lipid membrane to $\Delta G_{barrier} \sim 30\text{--}40 \text{ kJ/mol}$ will severely compromise the insulation properties of the phospholipid bilayer and result in an increase in membrane conductance. With the results derived in the previous paragraph, we are in a position to estimate membrane conductance from Eq. (7). The finding that a homogeneous membrane model cannot quantitatively account for the observed ion conduction suggests that A β_{1-42} oligomers form localized ion conduction pathways within a laterally inhomogeneous membrane. In the light of the activation energy results, these pathways cannot, however, be in the form of water-filled membrane-spanning channels. Equation (7) needs to be modified to describe such structural inhomogeneity in a parallel capacitor model. The parameter θ then determines the conductance, $Y = \theta \times Y_{A\beta}$, and yields $Y \approx 180 \mu\text{S}/\text{cm}^2$.⁸ This value is higher

the absence of the reversal potentials (17. Sokolov, Y., J. A. Kozak, R. Kaye, A. Chanturija, C. Glabe, and J. E. Hall. 2006. Soluble amyloid oligomers increase bilayer conductance by altering dielectric structure. *J. Gen. Physiol.* 128:637-647.) indicates that the permeability of Na^+ might be comparable to that of Cl^- . If so, the quantitative estimate for Y may be too low by up to a factor of $\sim 2x$.

⁷We note that generally, $E_a \neq \Delta G_{barrier}$. Instead, $E_a \approx \Delta H_{barrier}$, where H is enthalpy. However, because the activation energy is quite significant ($E_a > 10 RT$), and because Born theory doesn't account for chemical contributions to $\Delta G_{barrier}$, such as the entropy increase associated with ion dehydration upon partitioning into the membrane, we assume that $E_a \approx \Delta G_{barrier}$ is also valid for the purpose of this estimate.

⁸ $D = k_B T / (6\pi\eta r_{ion})$ yields $D_{Cl^-} = 3.95 \times 10^{-6} \text{ cm}^2/\text{s}$. $\Delta G_{barrier} = 36.8 \text{ kJ/mol}$, $d_{A\beta} = 3.28 \text{ nm}$. Na^+ contributions to the bilayer conductance are neglected.

than the experimental data presented in Fig. 6,⁹ but is nevertheless a realistic quantitative description of the physical situation given the substantial uncertainty of some of the input values. A similar analysis for free-standing BLMs in 10 mM electrolyte solution with the experimentally determined activation energy, $E_a \approx 39.4$ kJ/mol, yields a conductance of $6.3 \mu\text{S}/\text{cm}^2$ —close to the experimental results in Table 5.¹⁰

Implications for the molecular etiology of Alzheimer's disease. In a recent paper, Lashuel and Lansbury reviewed the available evidence for amyloid protofibrils as triggers of age-related neurodegenerative disease by induction of unregulated membrane permeabilization and pose the question (72), *Are amyloid diseases caused by aggregates that mimic bacterial pore-forming membranes?* In the data presented here, we see significant differences between the molecular mechanisms by which $A\beta$ oligomers on the one hand and on the other αHL or gramicidin D—prototypical and well-studied membrane pores—affect the membrane ion barrier. There is nevertheless ample evidence, following the seminal work by Arispe and collaborators (21,73), for amyloid-induced current traces reminiscent of channel-like conductance, as presented in various publications (23,24,74). Complementary morphological studies show AFM images in which donut-shaped peptide aggregates decorate bilayer surfaces (23-25), suggestive of pores perforating the underlying membranes. Further circumstantial evidence from blockage studies with specific metal ions such as Al^{3+} , Zn^{2+} or Cu^{2+} (73,75,76) lend even more credibility to the amyloid channel hypothesis. One has to keep in mind, however, that studies performed with $A\beta$ until recently were mostly ill-defined with respect to the peptides aggregation state, and peptide concentrations used in early work were often extremely high. With the exception of studies on acidic membranes (76), all the “classical” studies suggesting pore formation employed peptide concentrations which were at least 4x higher (24,25) than those in our experiments—and in many cases substantially more than that (58,73,74,77). On the other hand, physiological damage to cultured cells has been reported at peptide concentrations comparable with those used in this study (78,79).

The fact that E_a is c_p -dependent and the nearly quadratic dependence of $Y_{A\beta}$ on peptide concentration may hold important clues to the mode of action of the amyloid particles and possible conformational changes they incur in the membrane as a function of c_p . Clearly, we are at best in a very early stage toward unraveling the molecular details of how soluble $A\beta$ oligomers affect membranes, and in particular the c_p -dependencies of $Y_{A\beta}$ and E_a require careful investigation.

In addition to the use of well-defined $A\beta_{1-42}$ oligomer preparations at low concentrations, the current study also provides a novel approach to investigations on membrane-related issues concerning AD: It encompasses structural and functional characterization *of the same physical system*, as well as a quantitative comparison of the physical state of membranes before and during incubation with $A\beta_{1-42}$ oligomers. In distinction, earlier studies often used a variety of more indirect approaches to sample preparation, including the fusion of preformed peptide-lipid assembly products to membranes (73,75), crosslinking of amyloid multimers with glutaraldehyde (24), or—as in most AFM studies—premixing of lipid and peptide in organic solution and subsequent solvent evaporation (24,80). While the impact of these earlier studies on our

⁹The mean conductance of DOPC-based stBLMs obtained with different amyloid oligomer batches was $Y = 104 \pm 22 \mu\text{S}/\text{cm}^2$ ($n = 15$) at $c_p = 1.6 \mu\text{M}$. (The data set shown in Fig. 6 was at the low end of those results.) Therefore, the theoretically estimated conductance exceeds this mean value by a factor of 1.8.

¹⁰For BLMs neither reliable membrane capacitance data nor area fraction estimates exist for the presumed highly conducting membrane domains. In view of the lack of such information, by substituting stBLMs results into the estimate for the BLM, we assumed that the ϵ_{hc} increases by 13% in $A\beta$ -affected areas and that the surface fraction of $A\beta$ -induced domains in the membrane is $\theta \approx 0.06$.

thinking about amyloid-inferred membrane damage cannot be overstated, there has recently been substantial progress in the areas of biochemical synthesis and characterization and of physical characterization that enable a reinvestigation of the underlying mechanisms. Analogous to the realization, more than a decade ago, that the conspicuous fibrils are not the main pathologically active form of amyloid, another paradigm shift may just be beyond the horizon. One should therefore be open for a reassessment of the arguments that define the molecular mechanisms which lead to membrane damage in Alzheimer's disease.

CONCLUSIONS

Arrhenius plots of ion conductances across membranes show that amyloid-induced ion transport is fundamentally different from that through water-filled α HL pores or gramicidin channels: The activation energies for ion transport through membranes affected by A β oligomers is substantially higher than that found with α HL and gramicidin. In addition, E_a decreases with increasing amyloid concentration whereas it is approximately constant as a function of α HL concentration. The presence of a large barrier is also inferred from the exponential form of current-voltage curves (Fig. 7), which differ from the near-linear current-voltage characteristics of water-filled, low-barrier α HL pores reconstituted in membranes (81). The combination of precise experimental results for the membrane thickness and specific capacitance is in quantitative accord with a model in which A β_{1-42} oligomers insert into the bilayer membrane where they lead to domain formation. Amyloid oligomers may thereby create a mosaic with regions of high local dielectric constant—and consequently low dielectric barrier to ion transfer. Our present experiments cannot assess the size or distribution of these regions directly, but recent BLM experiments with conductance probes as well as work on Kv1.3 channels in living cells suggest that such regions of lower dielectric barrier may alter characteristic properties of a variety of ionophores and physiological ion channels in the membrane. Specifically, A β increases the conductance due to nonactin and tetraphenylborate in BLMs and accelerates the gating kinetics of the voltage-gated Kv1.3 channel in RBL cells (17). A β also increases the single-channel conductance of gramicidin channels and increases the efficiency of alamethicin (Sokolov and Hall, unpublished data). Thus A β oligomers alter the dielectric structure of the lipid bilayer in such a way as to facilitate charge translocation by a variety of conductance mechanisms. We suggest that such effects on the intrinsic membrane conductance and—more likely—on resident voltage-dependent proteins, such as synaptic Ca²⁺ channels (79), may well account for some of the toxic properties of soluble amyloid oligomers in Alzheimer's disease.

SUPPLEMENTARY MATERIAL

Supporting information associated with this article can be accessed at www.biophysj.org.

ACKNOWLEDGMENTS

Support by the National Institute of Standards and Technology (U.S. DOC) in providing the neutron research facilities used in this work is gratefully acknowledged. We benefited from helpful discussions with Charlie G. Glabe and valuable advice on A β oligomer preparation by Saskia C. Milton. Paul A. Kienzle provided support for the NR data analysis. This work was in parts funded by the NSF (CBET-0555201 and 0457148), the NIH (1 R01 RR14182), the Lithuanian State Science and Studies Foundation (B38/2008), the American Health Assistance Foundation (A2008-307), and the Alzheimer's Foundation (IIRG-06-26167).

REFERENCES

1. Cummings, B. J., C. J. Pike, R. Shankle, and C. W. Cotman. 1996. β -amyloid deposition and other measures of neuropathology predict cognitive status in Alzheimer's disease. *Neurobiol. Aging* 17:921-933.
2. Hardy, J. and D. J. Selkoe. 2002. Medicine - The amyloid hypothesis of Alzheimer's disease: Progress and problems on the road to therapeutics. *Science* 297:353-356.
3. Lansbury, P. T. and H. A. Lashuel. 2006. A century-old debate on protein aggregation and neurodegeneration enters the clinic. *Nature* 443:774-779.
4. Hardy, J. A. and G. A. Higgins. 1992. Alzheimers Disease - The amyloid cascade hypothesis. *Science* 256:184-185.
5. Temussi, P. A., L. Masino, and A. Pastore. 2003. From Alzheimer to Huntington: why is a structural understanding so difficult? *EMBO J.* 22:355-361.
6. Lindgren, M., K. Sörgjerd, and P. Hammarström. 2005. Detection and characterization of aggregates, prefibrillar amyloidogenic oligomers, and protofibrils using fluorescence spectroscopy. *Biophys. J.* 88:4200-4212.
7. Lührs, T., C. Ritter, M. Adrian, D. Riek-Loher, B. Bohrmann, H. Döbeli, D. Schubert, and R. Riek. 2005. 3D structure of Alzheimer's amyloid- β (1-42) fibrils. *Proc. Natl. Acad. Sci. USA* 102:17342-17347.
8. Mastrangelo, I. A., M. Ahmed, T. Sato, W. Liu, C. P. Wang, P. Hough, and S. O. Smith. 2006. High-resolution atomic force microscopy of soluble A β 42 oligomers. *J. Mol. Biol.* 358:106-119.
9. Chimon, S., M. A. Shaibat, C. R. Jones, D. C. Calero, B. Aizezi, and Y. Ishii. 2007. Evidence of fibril-like β -sheet structures in a neurotoxic amyloid intermediate of Alzheimer's β -amyloid. *Nat. Struct. Mol. Biol.* 14:1157-1164.
10. Kuo, Y. M., M. R. Emmerling, H. C. Lambert, S. R. Hempelman, T. A. Kokjohn, A. S. Woods, R. J. Cotter, and A. E. Roher. 1999. High levels of circulating A β 42 are sequestered by plasma proteins in Alzheimer's disease. *Biochem. Biophys. Res. Commun.* 257:787-791.
11. Lue, L. F., Y. M. Kuo, A. E. Roher, L. Brachova, Y. Shen, L. Sue, T. Beach, J. H. Kurth, R. E. Rydel, and J. Rogers. 1999. Soluble amyloid β peptide concentration as a predictor of synaptic change in Alzheimer's disease. *Am. J. Pathol.* 155:853-862.
12. McLean, C. A., R. A. Cherny, F. W. Fraser, S. J. Fuller, M. J. Smith, K. Beyreuther, A. I. Bush, and C. L. Masters. 1999. Soluble pool of A β amyloid as a determinant of severity of neurodegradation in Alzheimer's disease. *Ann. Neurol.* 46:860-866.
13. Walsh, D. M., I. Klyubin, J. V. Fadeeva, W. K. Cullen, R. Anwyl, M. S. Wolfe, M. J. Rowan, and D. J. Selkoe. 2002. Naturally secreted oligomers of amyloid β protein potently inhibit hippocampal long-term potentiation *in vivo*. *Nature* 416:535-539.
14. Kaye, R., E. Head, J. L. Thompson, T. M. McIntire, S. C. Milton, C. W. Cotman, and C. G. Glabe. 2003. Common structure of soluble amyloid oligomers implies common mechanism of pathogenesis. *Science* 300:486-489.

15. Kaye, R., Y. Sokolov, B. Edmonds, T. M. McIntire, S. C. Milton, J. E. Hall, and C. G. Glabe. 2004. Permeabilization of lipid bilayers is a common conformation-dependent activity of soluble amyloid oligomers in protein misfolding diseases. *J. Biol. Chem.* 279:46363-46366.
16. Guo, J. P., T. Arai, J. Miklossy, and P. L. McGeer. 2006. A β and tau form soluble complexes that may promote self aggregation of both into the insoluble forms observed in Alzheimer's disease. *Proc. Natl. Acad. Sci. USA* 103:1953-1958.
17. Sokolov, Y., J. A. Kozak, R. Kaye, A. Chanturija, C. Glabe, and J. E. Hall. 2006. Soluble amyloid oligomers increase bilayer conductance by altering dielectric structure. *J. Gen. Physiol.* 128:637-647.
18. Eliezer, D. 2006. Amyloid ion channels: A porous argument or a thin excuse? *J. Gen. Physiol.* 128:631-633.
19. Bucciantini, M., E. Giannoni, F. Chiti, F. Baroni, L. Formigli, J. S. Zurdo, N. Taddei, G. Ramponi, C. M. Dobson, and M. Stefani. 2002. Inherent toxicity of aggregates implies a common mechanism for protein misfolding diseases. *Nature* 416:507-511.
20. Ambroggio, E. E., D. H. Kim, F. Separovic, C. J. Barrow, K. J. Barnham, L. A. Bagatolli, and G. D. Fidelio. 2005. Surface behavior and lipid interaction of Alzheimer β -amyloid peptide 1–42: A membrane-disrupting peptide. *Biophys. J.* 88:2706 - 2713.
21. Arispe, N., H. B. Pollard, and E. Rojas. 1993. Giant multilevel cation channels formed by Alzheimer disease amyloid β protein [A β P(1-40)] in bilayer membranes. *Proc. Natl. Acad. Sci. USA* 90:10573-10577.
22. Kawahara, M. and Y. Kuroda. 2000. Molecular mechanism of neurodegeneration induced by Alzheimer's β -amyloid protein: Channel formation and disruption of calcium homeostasis. *Brain Res. Bull.* 53:389-397.
23. Lin, H., R. Bhatia, and R. Lal. 2001. Amyloid β protein forms ion channels: Implications for Alzheimer's disease pathophysiology. *FASEB J.* 15:2433-2444.
24. Quist, A., L. Doudevski, H. Lin, R. Azimova, D. Ng, B. Frangione, B. Kagan, J. Ghiso, and R. Lal. 2005. Amyloid ion channels: A common structural link for protein-misfolding disease. *Proc. Natl. Acad. Sci. USA* 102:10427-10432.
25. Green, J. D., L. Kreplak, C. Goldsbury, X. L. Blatter, M. Stolz, G. S. Cooper, A. Seelig, J. Kistler, and U. Aebi. 2004. Atomic force microscopy reveals defects within mica supported lipid bilayers induced by the amyloidogenic human amylin peptide. *J. Mol. Biol.* 342:877-887.
26. Micelli, S., D. Meleleo, V. Picciarelli, and E. Gallucci. 2004. Effect of sterols on β -amyloid peptide (A β P 1-40) channel formation and their properties in planar lipid membranes. *Biophys. J.* 86:2231-2237.
27. Kawahara, M., Y. Kuroda, N. Arispe, and E. Rojas. 2000. Alzheimer's β -amyloid, human islet amylin, and prion protein fragment evoke intracellular free calcium elevations by a common mechanism in a hypothalamic GnRH neuronal cell line. *J. Biol. Chem.* 275:14077-14083.
28. Bezrukov, S. M. and J. J. Kasianowicz. 1993. Current noise reveals protonation kinetics and number of ionizable sites in an open protein ion channel. *Phys. Rev. Lett.* 70:2352-2355.

29. Terzi, E., G. Hölzemann, and J. Seelig. 1997. Interaction of Alzheimer β -amyloid peptide(1-40) with lipid membranes. *Biochemistry* 36:14845-14852.
30. Yip, C. M. and J. McLaurin. 2001. Amyloid- β peptide assembly: A critical step in fibrillogenesis and membrane disruption. *Biophys. J.* 80:1359-1371.
31. Widenbrant, M. J. O., J. Rajadas, C. Sutardja, and G. G. Fuller. 2006. Lipid-induced β -amyloid peptide assemblage fragmentation. *Biophys. J.* 91:4071-4080.
32. Chi, E. Y., C. Ege, A. Winans, J. Majewski, G. Wu, K. Kjaer, and K. Y. C. Lee. 2008. Lipid membrane templates the ordering and induced fibrillogenesis of Alzheimer's disease amyloid- β peptide. *Proteins*:in press.
33. McIntosh, T. J. and S. A. Simon. 2006. Roles of bilayer material properties in function and distribution of membrane proteins. *Annu. Rev. Biophys. Biomol. Struct.* p 177-198.
34. Eehalt, R., P. Keller, C. Haass, C. Thiele, and K. Simons. 2003. Amyloidogenic processing of the Alzheimer β -amyloid precursor protein depends on lipid rafts. *J. Cell Biol.* 160:113-123.
35. Hur, J. Y., H. Welander, H. Behbahani, M. Aoki, J. Frånberg, B. Winblad, S. Frykman, and L. O. Tjernberg. 2008. Active γ -secretase is localized to detergent-resistant membranes in human brain. *FEBS J.* 275:1174-1187.
36. Hattori, C., M. Asai, H. Onishi, N. Sasagawa, Y. Hashimoto, T. C. Saido, K. Maruyama, S. Mizutani, and S. Ishiura. 2006. BACE1 interacts with lipid raft proteins. *J. Neurosci. Res.* 84:912-917.
37. Sackmann, E. 1996. Supported membranes - Scientific and practical applications. *Science* 271:43-48.
38. Cornell, B. A., V. L. B. Braach-Maksvytis, L. B. King, P. D. J. Osman, B. Raguse, L. Wiczorek, and R. J. Pace. 1997. A biosensor that uses ion-channel switches. *Nature* 387:580-583.
39. Tanaka, M. and E. Sackmann. 2005. Polymer-supported membranes as models of the cell surface. *Nature* 437:656-663.
40. McGillivray, D. J., G. Valincius, D. J. Vanderah, W. Febo-Ayala, J. T. Woodward, F. Heinrich, J. J. Kasianowicz, and M. Lösche. 2007. Molecular-scale structural and functional characterization of sparsely tethered bilayer lipid membranes. *Biointerphases* 2:21-33.
41. Valincius, G., D. J. McGillivray, W. Febo-Ayala, D. J. Vanderah, J. J. Kasianowicz, and M. Lösche. 2006. Enzyme activity to augment the characterization of tethered bilayer membranes. *J. Phys. Chem. B* 110:10213-10216.
42. Song, L., M. R. Hobaugh, C. Shustak, S. Cheley, H. Bayley, and J. E. Gouaux. 1996. Structure of staphylococcal α -hemolysin, a heptameric transmembrane pore. *Science* 274:1859-1865.
43. McGillivray, D. J., G. Valincius, F. Heinrich, J. W. F. Robertson, D. J. Vanderah, W. Febo-Ayala, I. Ignatjev, M. Lösche, and J. J. Kasianowicz. 2007. Functional reconstitution of *Staphylococcus aureus* α -hemolysin in tethered bilayer lipid membranes. Submitted.

44. Vanderah, D. J., C. W. Meuse, V. Silin, and A. L. Plant. 1998. Synthesis and characterization of self-assembled monolayers of alkylated 1-thiahexa(ethylene oxide) compounds on gold. *Langmuir* 14:6916-6923.
45. Demuro, A., E. Mina, R. Kayed, S. C. Milton, I. Parker, and C. G. Glabe. 2005. Calcium dysregulation and membrane disruption as a ubiquitous neurotoxic mechanism of soluble amyloid oligomers. *J. Biol. Chem.* 280:17294-17300.
46. Vanderah, D. J., R. S. Gates, V. Silin, D. N. Zeiger, J. T. Woodward, C. W. Meuse, G. Valincius, and B. Nickel. 2003. Isostructural self-assembled monolayers. 1. Octadecyl 1-thiaoligo(ethylene oxides). *Langmuir* 19:2612-2620.
47. Burstein, R. K. 1967. *Elektrokhimiya* 3:349.
48. Dura, J. A., D. Pierce, C. F. Majkrzak, N. Maliszewskyj, D. J. McGillivray, M. Lösche, K. V. O'Donovan, M. Mihailescu, U. A. Perez-Salas, D. L. Worcester, and S. H. White. 2006. AND/R: A neutron diffractometer/reflectometer for investigation of thin films and multilayers for the life sciences. *Rev. Sci. Instrum.* 77:074301.
49. Als-Nielsen, J. and K. Kjaer. 1989. X-ray reflectivity and diffraction studies of liquid surfaces and surfactant monolayers. In *Phase Transitions in Soft Condensed Matter*. T. Riste and D. Sherrington, editors. Plenum Press. New York. 113-138.
50. Kienzle, P. A., M. Doucet, D. J. McGillivray, K. V. O'Donovan, N. F. Berk, and C. F. Majkrzak. 2000-2006. ga_refl, <http://www.ncnr.nist.gov/reflpak/garefl.html>.
51. Parratt, L. G. 1954. Surface studies of solids by total reflection of x-rays. *Phys. Rev.* 95:359-369.
52. Vaknin, D., K. Kjaer, J. Als-Nielsen, and M. Lösche. 1991. Structural properties of phosphatidylcholine in a monolayer at the air/water interface. Neutron reflection study and reexamination of x-ray reflection experiments. *Biophys. J.* 59:1325-1332.
53. Wiener, M. C. and S. H. White. 1991. Fluid bilayer structure determination by the combined use of x-ray and neutron diffraction. II. "Composition-space" refinement method. *Biophys. J.* 59:174-185.
54. Cornell, B. A., G. Krishna, P. D. Osman, R. D. Pace, and L. Wiczorek. 2001. Tethered-bilayer lipid membranes as a support for membrane-active peptides. *Biochem. Soc. Trans.* 29:613-617.
55. Glazier, S. A., D. J. Vanderah, A. L. Plant, H. Bayley, G. Valincius, and J. J. Kasianowicz. 2000. Reconstitution of the pore-forming toxin α -hemolysin in phospholipid/18-octadecyl-1-thiahexa(ethylene oxide) and phospholipid/n-octadecanethiol supported bilayer membranes. *Langmuir* 16:10428-10435.
56. Kozak, J. A., Y. Sokolov, R. Kayed, C. Glabe, and J. E. Hall. 2007. Multiple effects of soluble amyloid peptide oligomers on human potassium channels. *Biophys. J.*:393A.
57. Chong, Y. H., Y. J. Shin, E. O. Lee, R. Kayed, C. G. Glabe, and A. J. Tenner. 2006. ERK1/2 activation mediates A beta oligomer-induced neurotoxicity via caspase-3 activation and tau cleavage in rat organotypic hippocampal slice cultures. *J. Biol. Chem.* 281:20315-20325.
58. Hirakura, Y., M. C. Lin, and B. L. Kagan. 1999. Alzheimer amyloid A β 1-42 channels: Effects of solvent, pH, and congo red. *J. Neurosci. Res.* 57:458-466.

59. Jang, H., J. Zheng, and R. Nussinov. 2007. Models of β -amyloid ion channels in the membrane suggest that channel formation in the bilayer is a dynamic process. *Biophys. J.* 93:1938-1949.
60. Kagan, B. L., Y. Hirakura, R. Azimov, R. Azimova, and M. C. Lin. 2002. The channel hypothesis of Alzheimer's disease: current status. *Peptides* 23:1311-1315.
61. Heller, W. T., A. J. Waring, R. I. Lehrer, T. A. Harroun, T. M. Weiss, L. Yang, and H. W. Huang. 2000. Membrane thinning effect of the β -sheet antimicrobial protegrin. *Biochemistry* 39:139-145.
62. Ludtke, S., K. He, and H. Huang. 1995. Membrane thinning caused by magainin 2. *Biochemistry* 34:16764-16769.
63. Chen, F. Y., M. T. Lee, and H. W. Huang. 2003. Evidence for membrane thinning effect as the mechanism for peptide-induced pore formation. *Biophys. J.* 84:3751-3758.
64. Gervasi, C. A. and A. E. Vallejo. 2002. Sodium ion transport through gramicidin-doped bilayers. Influences of temperature and ionic concentration. *Electrochim. Acta* 47:2259-2264.
65. Smart, O. S., J. M. Goodfellow, and B. A. Wallace. 1993. The pore dimensions of gramicidin A. *Biophys. J.* 65:2455-2460.
66. Wallace, B. A. 2000. Common structural features in gramicidin and other ion channels. *Bioessays* 22:227-234.
67. Walz, D., E. Bamberg, and P. Läuger. 1969. Nonlinear electrical effects in lipid bilayer membranes. 1. Ion injection. *Biophys. J.* 9:1150-1159.
68. Neumcke, B. and P. Läuger. 1969. Nonlinear electrical effects in lipid bilayer membranes. 2. Integration of generalized Nernst-Planck equations. *Biophys. J.* 9:1160-1170.
69. Parsegian, V. A. 1969. Energy of an ion crossing a low dielectric membrane - Solutions to 4 relevant electrostatic problems. *Nature* 221:844-846.
70. De Levie, R. 1978. Mathematical modeling of transport of lipid-soluble ions and ion-carrier complexes through lipid bilayer membranes. *Adv. Chem. Phys.* 37:99-137.
71. Dilger, J. P., S. G. A. McLaughlin, T. J. McIntosh, and S. A. Simon. 1979. Dielectric constant of phospholipid bilayers and the permeability of membranes to ions. *Science* 206:1196-1198.
72. Lashuel, H. A. and P. T. Lansbury. 2006. Are amyloid diseases caused by protein aggregates that mimic bacterial pore-forming toxins? *Quart. Rev. Biophys.* 39:167-201.
73. Arispe, N., E. Rojas, and H. B. Pollard. 1993. Alzheimer disease amyloid β protein forms calcium channels in bilayer membranes: Blockade by tromethamine and aluminum. *Proc. Natl. Acad. Sci. USA* 90:567-571.
74. Kawahara, M., N. Arispe, Y. Kuroda, and E. Rojas. 1997. Alzheimer's disease amyloid β protein forms Zn^{2+} -sensitive, cation-selective channels across excised membrane patches from hypothalamic neurons. *Biophys. J.* 73:67-75.
75. Arispe, N., H. B. Pollard, and E. Rojas. 1996. Zn^{2+} interaction with Alzheimer amyloid β protein calcium channels. *Proc. Natl. Acad. Sci. USA* 93:1710-1715.

76. Bahadi, R., P. V. Farrelly, B. L. Kenna, C. C. Curtain, C. L. Masters, R. Cappai, K. J. Barnham, and J. I. Kourie. 2003. Cu^{2+} -induced modification of the kinetics of $\text{A}\beta(1-42)$ channels. *Am. J. Physiol.-Cell Physiol.* 285:C873-C880.
77. Singer, S. J. and N. N. Dewji. 2006. Evidence that Perutz's double- β -stranded subunit structure for β -amyloids also applies to their channel-forming structures in membranes. *Proc. Natl. Acad. Sci. USA* 103:1546-1550.
78. Bhatia, R., H. Lin, and R. Lal. 2000. Fresh and globular amyloid β protein (1-42) induces rapid cellular degeneration: Evidence for $\text{A}\beta\text{P}$ channel-mediated cellular toxicity. *FASEB J.* 14:1233-1243.
79. MacManus, A., M. Ramsden, M. Murray, Z. Henderson, H. A. Pearson, and V. A. Campbell. 2000. Enhancement of $^{45}\text{Ca}^{2+}$ influx and voltage-dependent Ca^{2+} channel activity by β -amyloid-(1-40) in rat cortical synaptosomes and cultured cortical neurons - Modulation by the proinflammatory cytokine interleukin-1 β . *J. Biol. Chem.* 275:4713-4718.
80. Lin, B., T. L. Morkved, M. Meron, Z. Q. Huang, P. J. Viccaro, H. M. Jaeger, S. M. Williams, and M. L. Schlossman. 1999. X-ray studies of polymer/gold nonocomposites. *J. Appl. Phys.* 85:3180-3184.
81. Misakian, M., J. J. Kasianowicz, B. Robertson, and O. Petersons. 2001. Frequency response of alternating currents through the *Staphylococcus aureus* α -hemolysin ion channel. *Bioelectromagnetics* 22:487-493.

TABLES

Table 1: Model parameters describing changes of an stBLM structure (WC14: β ME = 3:7 + DMPC-d₅₄) upon incubation with soluble prefibrillar A β ₁₋₄₂ oligomers.

	neat bilayer	change from neat bilayer	2 μ M A β ₁₋₄₂	6 μ M A β ₁₋₄₂	12 μ M A β ₁₋₄₂	rinse
thickness of tether layer (Å)	10.5±1.7					
thickness of each bilayer leaflet (Å)	14.9±1.2	change:	0.0±0.2	-0.7±0.2	-1.5±0.2	-0.3±0.2
thickness of headgroup layer (Å)	7.0 (fixed)					
volume fraction of tether in layer	0.69±0.02					
volume fraction inner lipid leaflet	0.93±0.04	change:	-0.01±0.02	0.0±0.03	+0.02±0.03	+0.01±0.03
volume fraction outer lipid leaflet	0.95±0.02	change:	+0.01±0.02	-0.01±0.03	-0.01±0.03	0.0±0.03
volume fraction outer headgroup	0.59±0.09	change:	+0.08±0.04	+0.06±0.04	+0.08±0.05	0.0±0.05
nSLD inner lipid leaflet (10 ⁻⁶ Å ⁻²)	1.60±0.13	change:	+0.29±0.09	+0.24±0.09	+0.08±0.09	+0.03±0.10
nSLD outer lipid leaflet (10 ⁻⁶ Å ⁻²)	5.55±0.34	change:	+0.29±0.08	+0.49±0.11	+0.48±0.18	+0.09±0.11
substrate roughness (Å)	3.96±1.29					
bilayer roughness (Å)	7.89±1.99					
χ^2	5.4, 2.5, 1.6		3.7, 2.4	2.6, 2.0, 1.8	2.4, 2.0	3.0, 1.8

Table 2: Model parameters describing changes of an stBLM structure (WC14: β ME = 3:7 + DOPC) upon incubation with soluble prefibrillar A β_{1-42} oligomers.

	neat bilayer	change from neat bilayer	6 μ M A β_{1-42}	12 μ M A β_{1-42}	rinse
thickness of tether layer (\AA)	11.3 \pm 1.0				
thickness of both bilayer leaflets (\AA)	31.0 \pm 0.6	change:	-2.4 \pm 0.6	-3.8 \pm 0.6	0.0 \pm 0.6
thickness of headgroup layer (\AA)	7.0 (fixed)				
volume fraction of tether in layer	0.59 \pm 0.02				
volume fraction inner lipid leaflet	1.00 \pm 0.02	change:	-0.01 \pm 0.02	0.00 \pm 0.03	-0.01 \pm 0.02
volume fraction outer lipid leaflet	1.00 \pm 0.02	change:	0.00 \pm 0.02	0.00 \pm 0.03	-0.02 \pm 0.02
volume fraction outer headgroup	0.66 \pm 0.10	change:	0.05 \pm 0.10	+0.05 \pm 0.10	-0.02 \pm 0.10
nSLD of both lipid leaflets (10^{-6}\AA^{-2})	-0.15 \pm 0.08	change:	+0.15 \pm 0.06	+0.19 \pm 0.06	+0.02 \pm 0.06
bilayer roughness (\AA)	6.5 \pm 2.2				
χ^2	3.30				

Table 3: Model parameters describing changes of an stBLM structure (WC14: β ME = 3:7 + DPhyPC) upon incubation with soluble prefibrillar $A\beta_{1-42}$ oligomers.

	neat bilayer	change from neat bilayer	6 μ M $A\beta_{1-42}$	rinse
thickness of tether layer (\AA)	14.0 \pm 1.5			
thickness of both bilayer leaflets (\AA)	28.6 \pm 1.4	change:	+0.2 \pm 0.4	-0.4 \pm 0.4
thickness of headgroup layer (\AA)	7.0 (fixed)			
volume fraction of tether in layer	0.66 \pm 0.04			
volume fraction inner lipid leaflet	1.00 \pm 0.04			
volume fraction outer lipid leaflet	1.00 \pm 0.01			
volume fraction outer headgroup	0.42 \pm 0.12			
nSLD of both lipid leaflets (10^{-6}\AA^{-2})	-0.31 \pm 0.09	change:	+0.12 \pm 0.05	-0.02 \pm 0.05
bilayer roughness (\AA)	6.4 \pm 3.1			
χ^2	3.06			

Table 4: EIS model fits (ECM shown in Fig. 5; $f = 1 \text{ Hz to } 33 \text{ kHz}$) for an stBLM (WC14: β ME = 3:7 + DOPC) as prepared and after incubation with soluble prefibrillar $A\beta_{1-42}$ oligomers. Shown are averages and standard deviations from multiple measurements ($n > 10$).

	neat bilayer	1.61 μ M $A\beta_{1-42}$	rinse
CPE_{stBLM} ($\mu\text{F}/\text{cm}^2\text{s}^{(\alpha-1)}$)	0.676 \pm 0.015	0.743 \pm 0.018	0.672 \pm 0.024
α_{stBLM}	0.987 \pm 0.002	0.979 \pm 0.002	0.985 \pm 0.002
CPE_{def} ($\mu\text{F}/\text{cm}^2\text{s}^{(\alpha-1)}$)	1.01 \pm 0.22	2.36 \pm 0.46	1.11 \pm 0.21
α_{def}	0.52 \pm 0.08	0.93 \pm 0.04	0.55 \pm 0.06
R_{def} ($\text{k}\Omega\text{cm}^2$)	933 \pm 110	9.6 \pm 2.7	645 \pm 124

Table 5: Zero-voltage conductances of free-standing BLMs as a function of T , calculated from $U \rightarrow 0$ in the current-voltage curves shown in Figure 7.

Temperature, T ($^{\circ}\text{C}$)	specific conductance, Y ($\mu\text{S cm}^{-2}$)	
	1 $\mu\text{M A}\beta_{1-42}$	2 $\mu\text{M A}\beta_{1-42}$
10	0.49	3.84
20	1.14	5.73
30	1.68	8.10
40	3.49	15.1

Table 6: Activation energies determined from the Arrhenius plots shown in Figure 9. A comparison between $\text{A}\beta$ -induced conductances, the conductance induced by the pore-forming α -hemolysin and the conductance of ions in bulk solution reveals that the ion transfer mechanisms induced by soluble $\text{A}\beta_{1-42}$ oligomers is substantially different from that through αHL .

system (experimental conditions)	activation energy, ΔE (kJ/mol)
1.6 $\mu\text{M A}\beta_{1-42}$ oligomers in stBLMs (EIS, 100 mM NaCl)	36.8
1 $\mu\text{M A}\beta_{1-42}$ oligomers in BLMs (current, 10 mM NaCl)	46.1
2 $\mu\text{M A}\beta_{1-42}$ oligomers in BLMs (current, 10 mM NaCl)	32.7
αHL in stBLMs (EIS, 100 mM NaCl)	9.9
100 μM gramicidin D (EIS, 100 mM NaCl)	16.7 [‡]
100 mM NaCl solution (EIS)	5.6 ... 6.5

[‡]see Gervasi and Vallejo, ref. (64)

FIGURE LEGENDS

Figure 1: Schematic representation of the synthetic lipid bilayer systems used in this study. (A) Free-standing BLM; (B) Solid-supported stBLM. Molecular details of stBLMs, specifically the geometry and hydration of the submembrane space between the bilayer and the inorganic substrate, have been established with NR in earlier work (40,41) and are drawn to scale.

Figure 2: Neutron reflection of an stBLM (WC14: β ME = 3:7 + DMPC- d_{54}), and changes in bilayer structure introduced by $A\beta_{1-42}$ oligomers. Out of a multitude of NR data sets, collected with the same bilayer with various solvent contrasts (see text), two exemplary data sets (as-prepared stBLM and the same stBLM in contact with dissolved $A\beta$ oligomers, $c_p = 12 \mu\text{M}$ of peptide) are shown in the main panel. Both data sets were measured in H_2O -based buffer. The prominently visible interference patterns are primarily due to the gold layer. If visually inspected, any organic interface layer alters this interference pattern only slightly. However, these changes are much larger than the precision of the data (error bars are shown for every data point; at low Q_z , errors are generally much smaller than plot symbols). The significance of the changes in reflectivity due to bilayers with different structure is emphasized in a residuals plot (lower inset) in which deviations of the data set shown in as gray triangles ($12 \mu\text{M}$ $A\beta$) from the data shown as black circles (neat stBLM) are plotted. The residuals of an NR spectrum for the amyloid-incubated stBLM after a buffer rinse are also shown (thin black line), indicating the reversibility of structural changes. The upper inset shows the modeled nSLD profiles of the organic interface layers (Si substrate, SiO_x layer, Cr bonding layer, and Au layer are partially omitted). These models have been derived from multiple solvent contrasts for which the data are not shown. The reflectivities computed for the shown nSLD profiles overlay the data points in the main panel as solid (black) or broken (gray) lines. A color version of this figure is available as Supplemental Material.

Figure 3: Neutron reflection of an stBLM (WC14: β ME = 3:7 + DOPC), and changes in bilayer structure introduced by $A\beta_{1-42}$ oligomers. Out of a multitude of NR data sets, collected with the same bilayer with various solvent contrasts, two exemplary data sets (as-prepared stBLM and the same stBLM in contact with dissolved $A\beta$ oligomers, $c_p = 12 \mu\text{M}$ of peptide) are shown in the main panel. Both data sets were measured in D_2O -based buffer. Because peptide in H_2O was added to the buffer, its nSLD is lower than that of the peptide-free buffer (see upper inset). The resulting difference in scattering power of the solvent leads to a difference in nSLD at the location of the HEO tether, showing that the tether region is hydrated. Other details of the presentation are as described for Fig. 2. A color version of this figure is available as Supplemental Material.

Figure 4: Neutron reflection of an stBLM (WC14: β ME = 3:7 + DPhyPC), and changes in bilayer structure introduced by $A\beta_{1-42}$ oligomers. Out of a multitude of NR data sets, collected with the same bilayer with various solvent contrasts, two exemplary data sets (as-prepared stBLM and the same stBLM in contact with dissolved $A\beta$ oligomers, $c_p = 6 \mu\text{M}$ of peptide) are shown in the main panel. Both data sets were measured in D_2O -based buffer. Because peptide in H_2O was added to the buffer, its nSLD is lower than that of the peptide-free buffer (see upper inset). The resulting difference in scattering power of the solvent leads to a difference in nSLD at the location of the HEO tether, showing that the tether region is hydrated. Other details of the

presentation are as described for Fig. 2. A color version of this figure is available as Supplemental Material.

Figure 5: Electrochemical impedance spectra (A: modulus, B: phase angle) of an stBLM (WC14: β ME = 3:7 + DOPC) in phosphate-buffered NaCl (0.1 M), pH 7.4, as a function of peptide concentration. Solid traces: no peptide. Short dashes: 0.48 μ M $A\beta_{1-42}$. Dash-dotted traces: 0.75 μ M $A\beta_{1-42}$. Long dashes: 1.61 μ M $A\beta_{1-42}$. Inset: ECM used to model stBLM data such as those shown in the main panel. “CPE” denotes constant phase elements. The subscript “def” denotes peptide-induced defect conductance pathways. Details, see text.

Figure 6: Impact of soluble prefibrillar $A\beta_{1-42}$ oligomers on membrane capacitance and conductance in an stBLM (WC14: β ME = 3:7 + DOPC; 0.1 M NaCl, pH 7.5) as a function of peptide concentration, measured on one single bilayer. Circles/solid line: stBLM capacitance. Squares/dashed line: stBLM conductance. Circles/squares: best-fit parameters from a model (ECM in the inset in Fig. 5) that describe data sets such as those shown in the main panel of Fig. 5.

Figure 7: Temperature dependence of current-voltage curves recorded on free-standing DOPC BLMs (10 mM KCl, 1 mM HEPES-Tris, pH=7.5) incubated with soluble prefibrillar $A\beta_{1-42}$ oligomers at a total peptide concentration of 1 μ M. Voltage scan rate: 30 mV/s. The inset shows an enlarged view of the data in the main panel near zero voltage.

Figure 8: Effect of soluble prefibrillar $A\beta_{1-42}$ oligomers on the conductance of free-standing BLMs (10 mM KCl, 1 mM HEPES-Tris, pH=7.5, $T = 25^\circ\text{C}$) as a function of lipid composition. $U = +150$ mV in all measurements.

Figure 9: Arrhenius plots of ion conductances across bilayers, induced by soluble prefibrillar $A\beta_{1-42}$ oligomers or by α -hemolysin, and in the electrolytes bathing these bilayers. In stBLMs, the conductances were derived from modeling EIS data with the ECM shown as an inset in Fig. 5. Therefore, bulk electrolyte conductances (filled squares and circles) and membrane conductances (empty squares and circles) were determined in the same experiment. The stBLM incubated with $A\beta$ (circles) was composed of WC14: β ME = 3:7 + DOPC; 0.1 M NaCl, pH 7.5. The stBLM reconstituted with α HL (squares) was prepared as described (40) and consisted of WC14: β ME = 3:7 + DPhyPC. Measurements on free-standing BLMs (triangles) were conducted with DOPC membranes in 10 mM KCl, HEPES-Tris, pH 7.4. $R = 8.3145$ J/(mol \times K) is the gas constant. Lines are best fits to the data.

Figure 10: Structural changes of an stBLM (WC14: β ME = 3:7 + DMPC-d₅₄) upon incubation with soluble prefibrillar $A\beta_{1-42}$ oligomers at various concentrations, and subsequent rinsing with peptide-free buffer. The plots visualize the development of model parameters, derived from simultaneous fits to multiple data sets, as a function of c_p . A: Changes of the nSLD in apposed bilayer leaflets. Note that the baseline nSLD is different in the two leaflets (c.f. Fig. 2, upper inset). B: Changes in layer thickness. For the peptide concentration, $c_p = 12$ μ M, the reduction in layer thickness is visualized in the upper inset in Fig. 2. C: Changes in neutron scattering length per unit area, discriminated by apposed leaflets. In A and C, triangles and squares refer to the inner and outer bilayer leaflet, respectively. In B, leaflets are not discriminated. In panel C, the respective changes for various values of c_p fall on top of each other for the two leaflets within confidence limits. Dashed lines are guides for the eye.

FIGURES

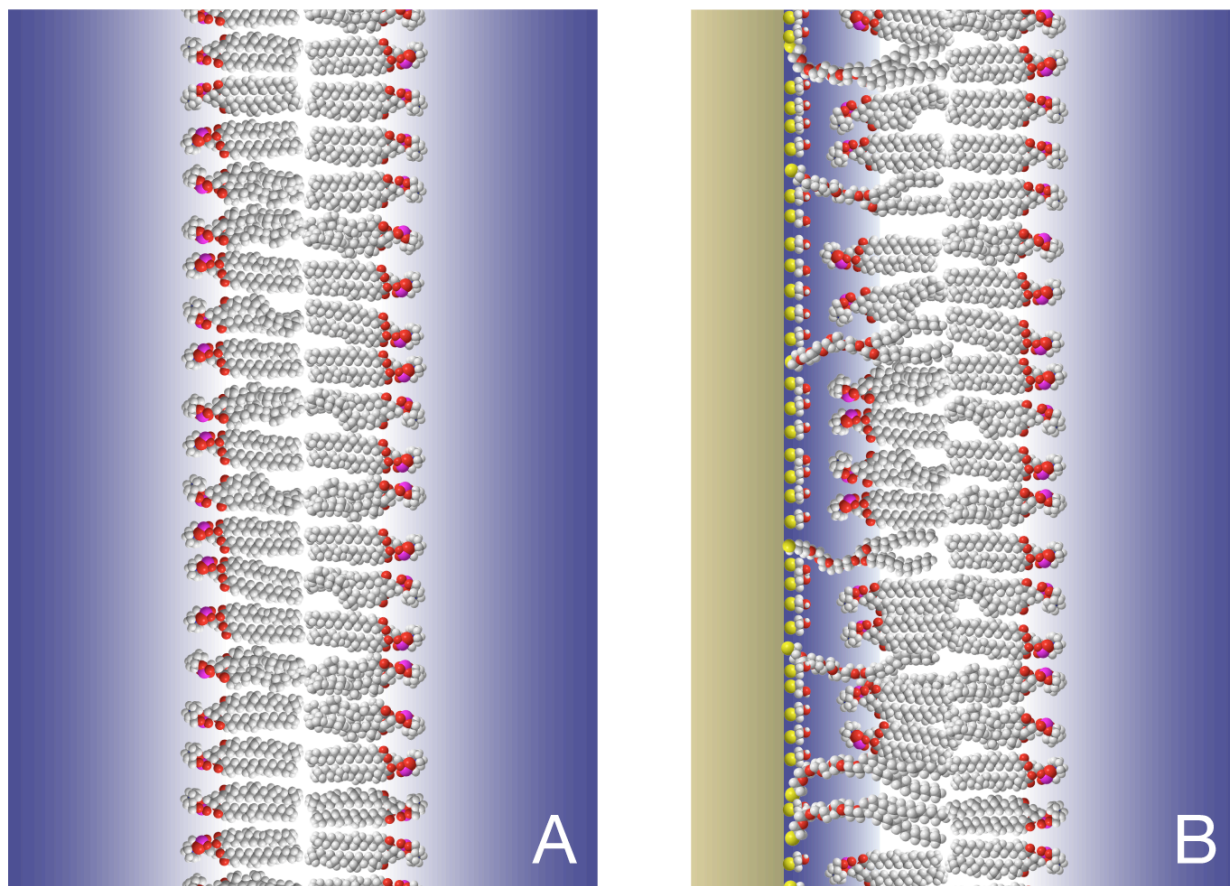


Figure 1

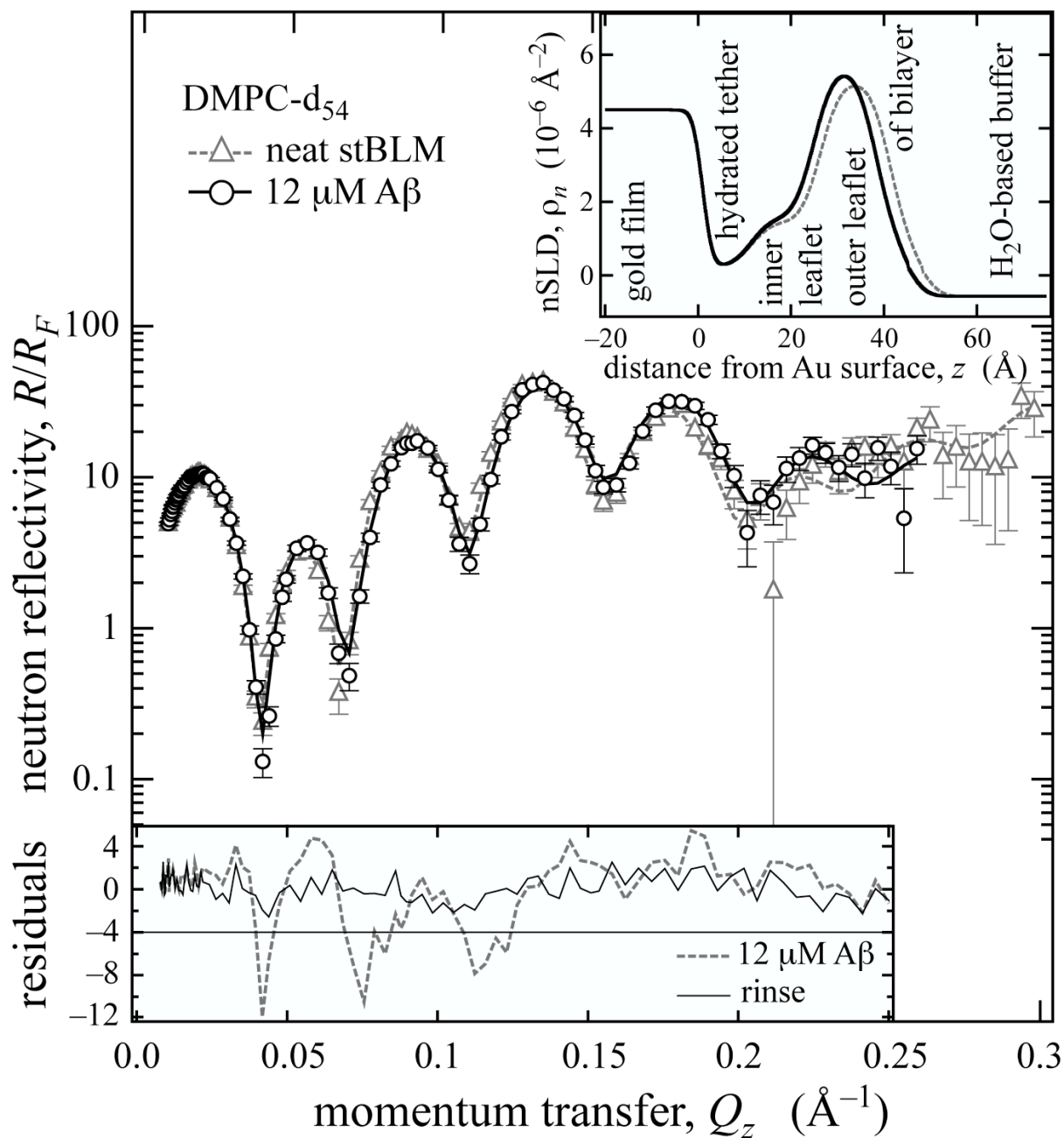


Figure 2

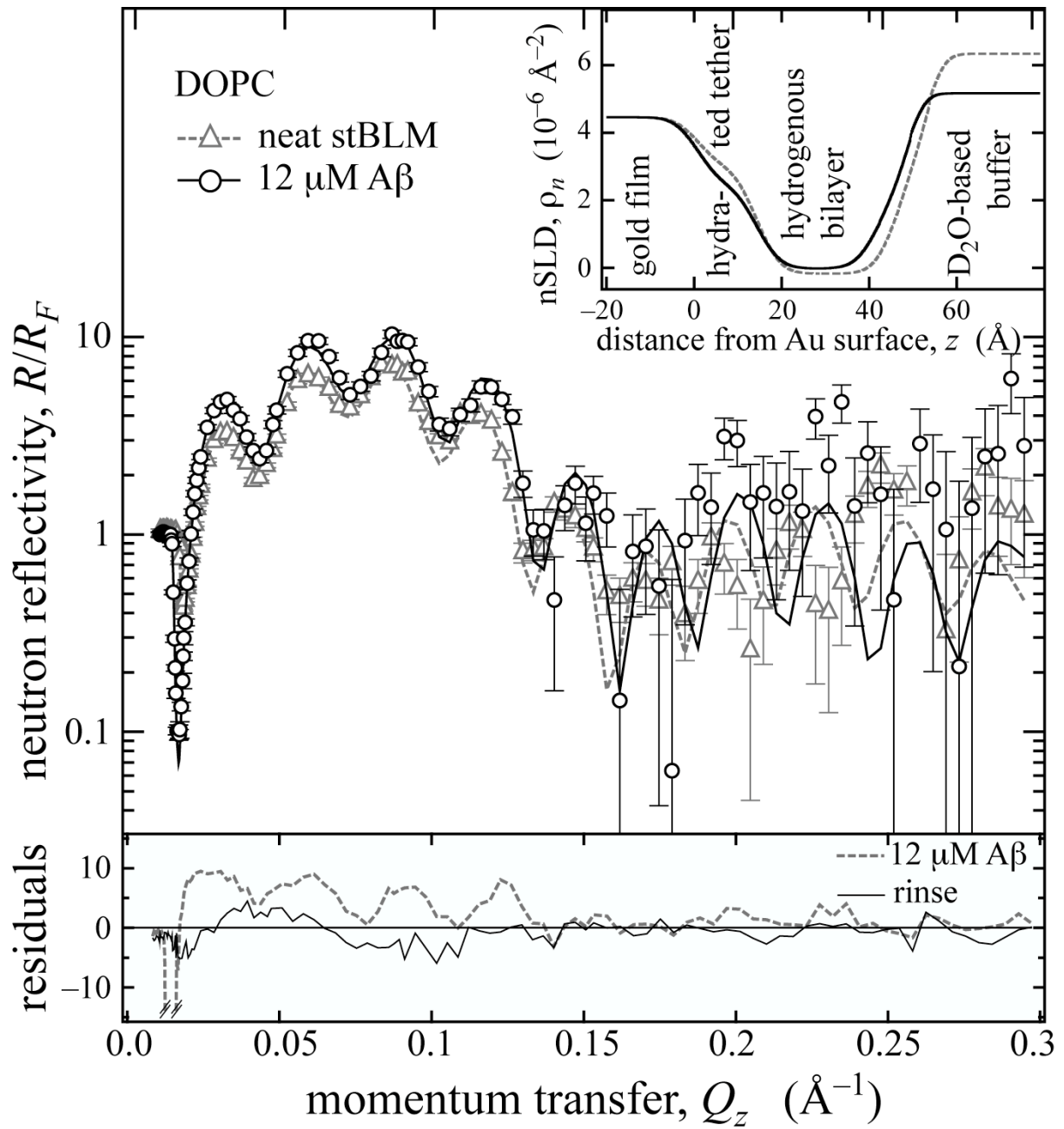


Figure 3

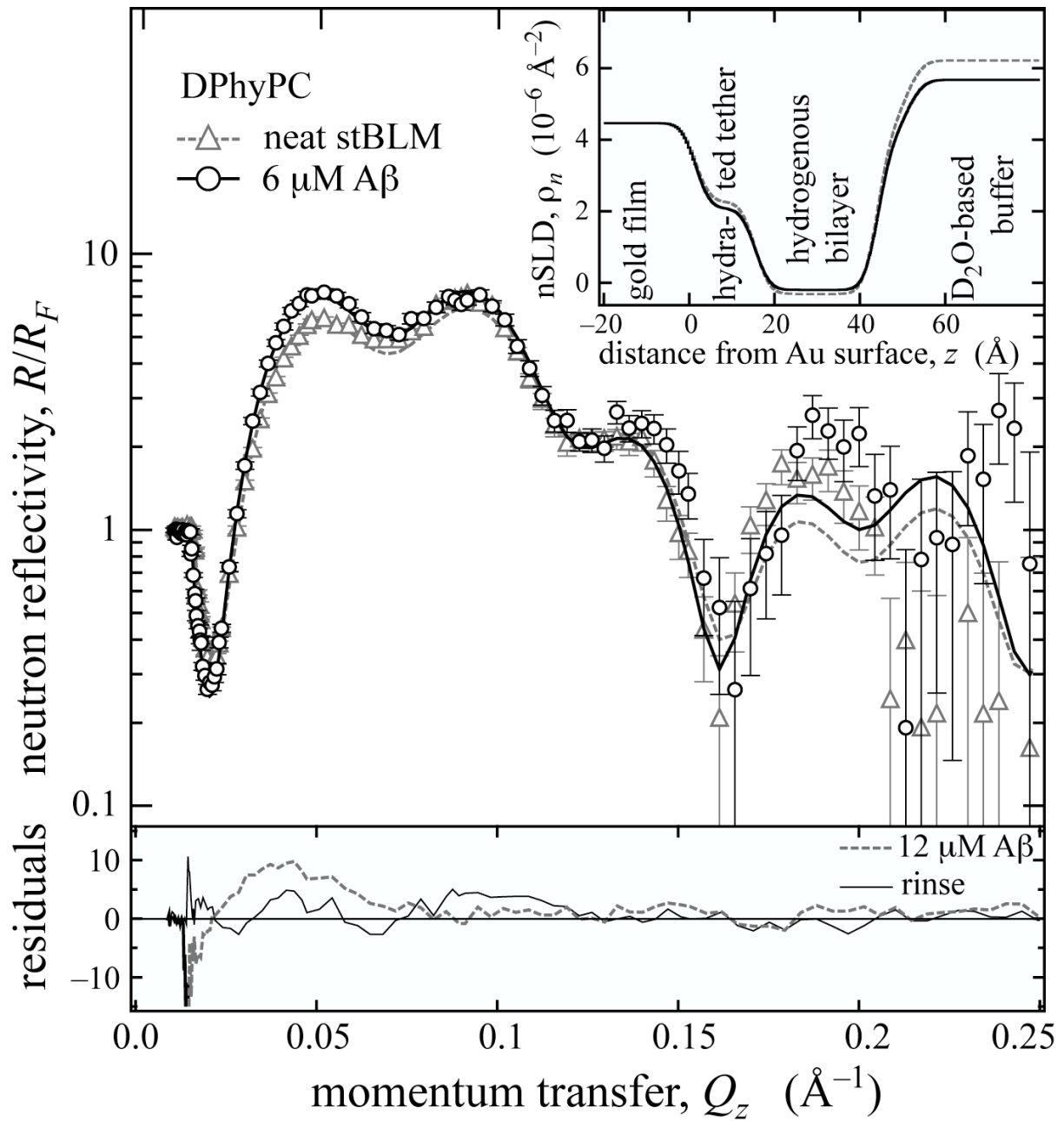


Figure 4

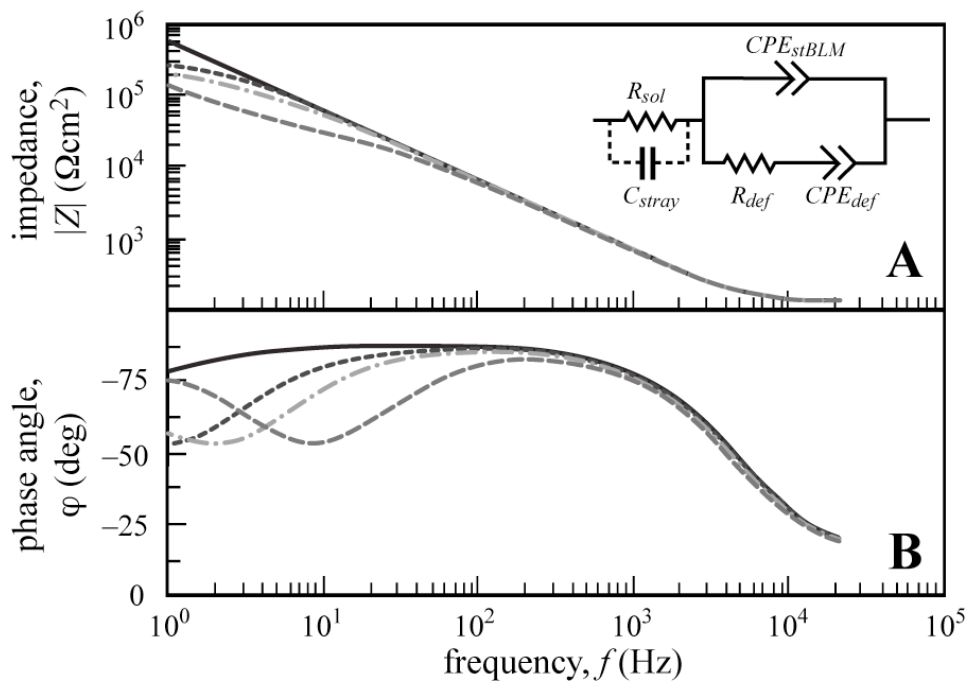


Figure 5

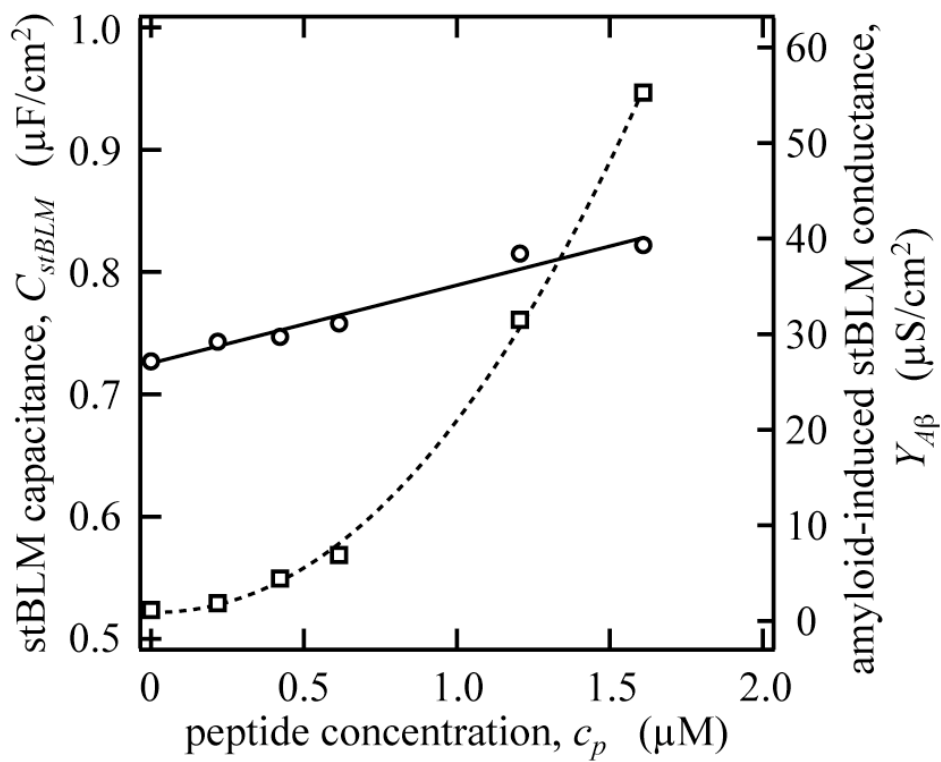


Figure 6

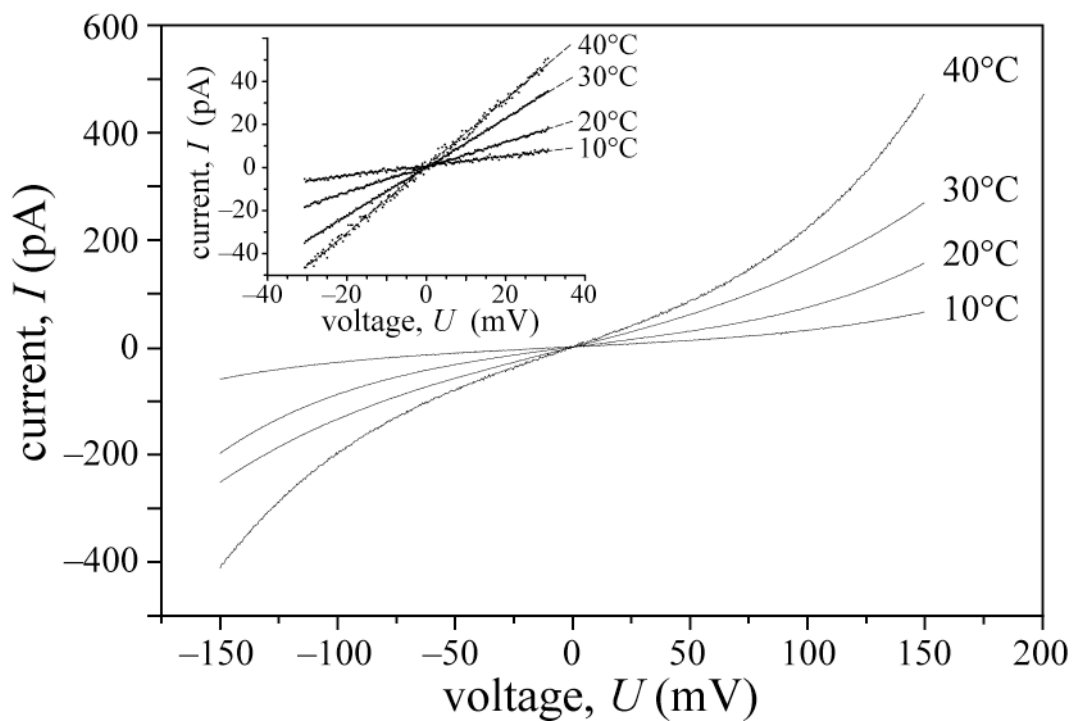


Figure 7

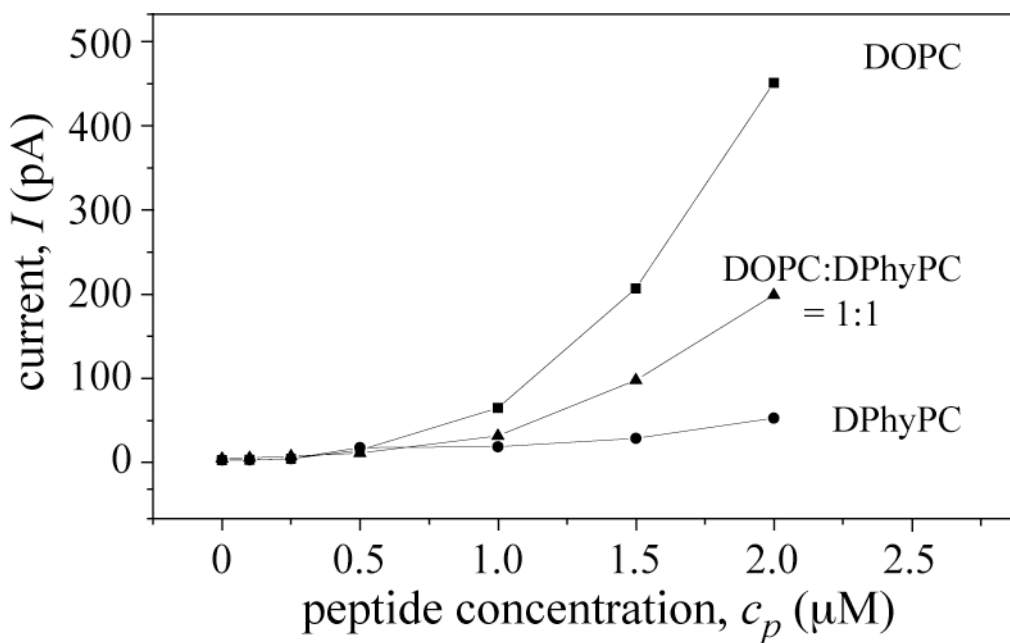


Figure 8

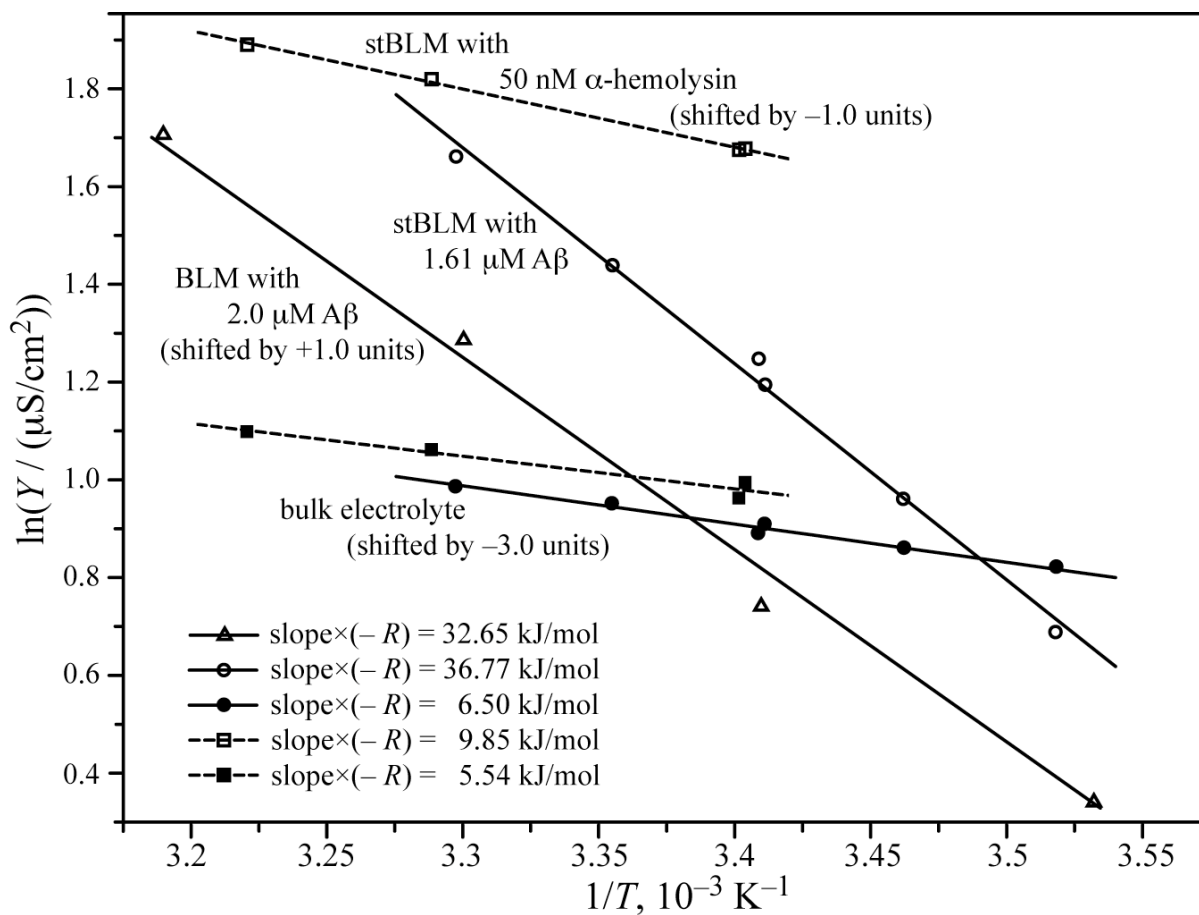


Figure 9

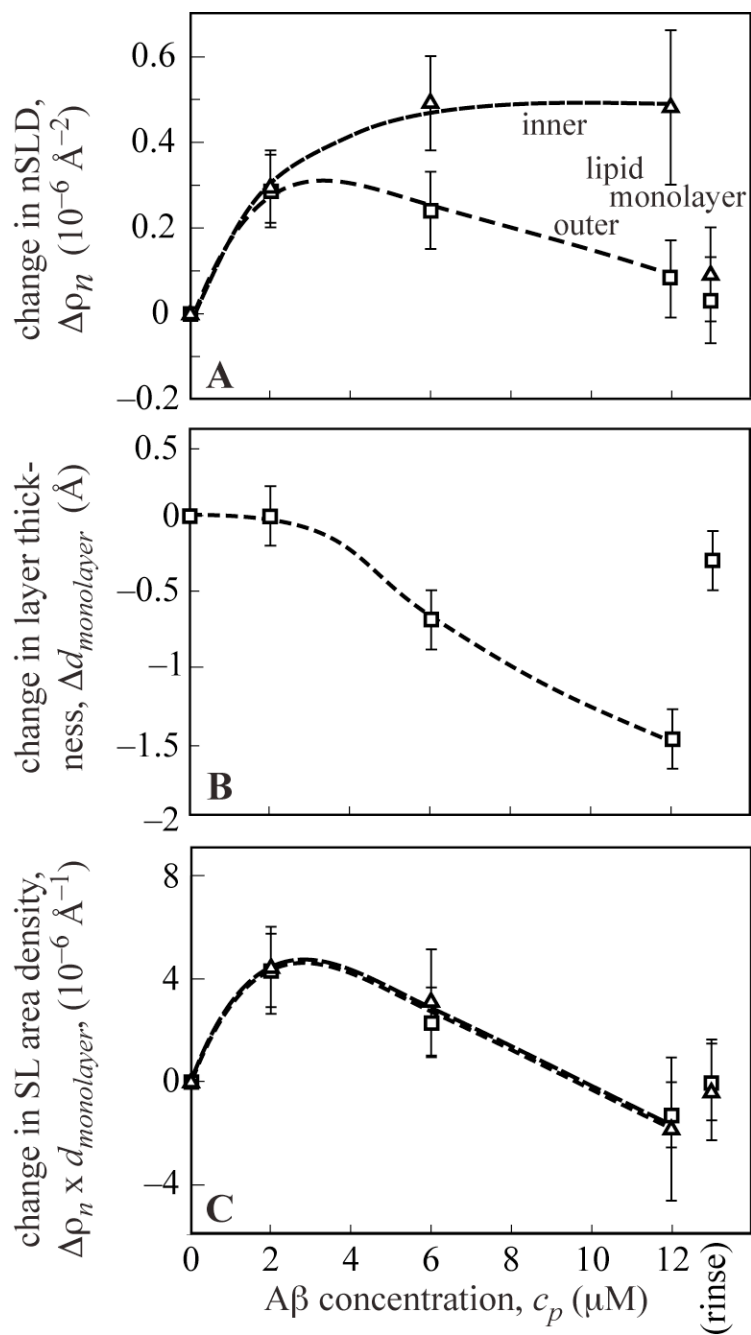


Figure 10